

The GISS Global Climate–Middle Atmosphere Model. Part I: Model Structure and Climatology

D. RIND, R. SUOZZO*, N. K. BALACHANDRAN**, A. LACIS AND G. RUSSELL

Goddard Space Flight Center, Institute for Space Studies, New York, NY

(Manuscript received 3 April 1987, in final form 20 August 1987)

ABSTRACT

The GISS global climate model (Hansen et al.) has been extended to include the middle atmosphere up to an altitude of approximately 85 km. The model has the full array of processes used for climate research, i.e., numerical solutions of the primitive equations, calculation of radiative and surface fluxes, a complete hydrologic cycle with convective and cloud cover parameterizations, etc. In addition, a parameterized gravity wave drag formulation has been incorporated, in which gravity-wave momentum fluxes due to flow over topography, wind shear and convection are calculated at each grid box, using theoretical relationships between the grid-scale variables and expected source strengths. The parameterized waves then propagate vertically upward depending on the instantaneous wind and temperature profiles, with waves breaking at levels in which their momentum flux exceeds the background saturation value. Radiative damping is also calculated, and the total momentum convergence in each layer is used to alter the local wind, while the kinetic energy dissipation warms the temperature. Thus the generation, propagation, breaking and drag are all a function of the calculated variables at each grid box for the various vertical levels.

The model has been run for five years, and the results compared with observations. The model produces generally realistic fields of temperature and wind throughout the atmosphere up to approximately 75 km. Important aspects of the current simulation include a proper break between the tropospheric and stratospheric jets, realistic closing off of the wintertime jet in the mesosphere, the observed warm winter/cold summer mesosphere, and a semiannual wind oscillation near the stratopause. The most obvious deficiencies are that the long-wave energy itself is somewhat too small in the low and midstratosphere, temperatures are too cold near the model top and are too warm in the polar Southern Hemisphere lower stratosphere during winter. Also, the model generates an inertial oscillation near the equatorial stratopause which may be excessive. Experiments are run without the various gravity wave drag mechanisms to quantify their effects. It is shown that a coarse-grid general circulation model with parameterized gravity-wave drag can produce a reasonable simulation of the middle atmosphere, which makes possible relatively long-term integrations.

1. Introduction

There is great incentive for developing global climate/middle atmosphere models (GCMAM) which would include a realistic representation of tropospheric climate and at the same time accurately reproduce the middle atmosphere (defined here as the region from approximately 10–100 km). This is due to the increasing recognition that climate changes will alter the stratosphere—either directly through the effect of increasing CO₂ (or water vapor) on stratospheric temperatures, or through climatic effects on planetary wave generation and propagation. In addition, changes in stratospheric trace gases have the potential to influence

tropospheric climate (e.g., Lacis et al., 1981; Ramanathan et al., 1985). Understanding the future trends of either the climate system or the stratosphere thus involves the development of coupled climate/middle atmosphere models.

Assessment of the equilibrium response of the climate system to perturbations requires multiyear simulations of global climate models, as the thermal inertia of the oceans necessitates runs of some 30 model years to reach equilibrium. Simulations of the transient response of the system for the next few decades entails a similar computational load. It is thus important to determine what spatial resolution is required in developing a coupled model, for the additional layers involved in simulating the stratosphere and mesosphere make even short-term integrations costly.

At first glance the stratosphere would seem to be the ideal location for coarse-grid models. The dynamics is dominated by wavenumbers 1 and 2, and small-scale phenomena had been thought to play a negligible role. However, additional modeling experience has caused this view to be revised. It appears as if coarse-grid mod-

* Sigma Data Service Corporation, New York, NY 10025.

** Lamont-Doherty Geological Observatory of Columbia University, Palisades, NY 10964.

Corresponding author address: Dr. David Rind, Goddard Space Flight Center, Institute for Space Studies, 2880 Broadway (Room 636), New York, NY 10023.

els have difficulty in generating the proper long-wave energy (in wavenumbers 1–4) in the troposphere (e.g., Miyakoda et al., 1972), which then affects the stratospheric model. The reason for this difficulty is not yet understood; it may have to do with the imprecision with which mountains are resolved when the resolution is too coarse, or it may be associated with improper nonlinear energy transfers from smaller-scale fast-moving waves, poorly resolved in coarse-grid models (Itoh, 1985). At this time even finer-grid models have difficulty generating proper long-wave energy distributions (Wallace and Woessner, 1981), which indicates that spatial resolution is just one of the factors that impact long-wave modeling.

In addition, it is now believed that small-scale effects lead to kinetic energy dissipation which is involved in closing off the stratospheric jet, and possibly the tropospheric jet (e.g., Lindzen, 1985). This dissipation is thought to be the result of gravity wave breaking in the mesosphere and stratosphere. There are some observations indicating wave-breaking phenomena (e.g., Lilly and Lester, 1974; Balsley et al., 1983; Vincent, 1984), although the actual dissipation which results from gravity-wave breaking has only been crudely estimated; studies indicate decelerations of the zonal winds of the order of a few tens of meters per second per day (Vincent and Reid, 1983; Fritts et al., 1984). While the prevailing view is that gravity-wave breaking is the best candidate for supplying the necessary dissipation, other phenomena such as inertial instability may act at specific low latitudes (Dunkerton, 1981).

Various quasi-geostrophic and two-dimensional models have now incorporated a gravity-wave drag formulation to improve middle atmosphere simulations (e.g., Holton, 1983), and Kida (1984) prescribed randomly generated gravity wave sources at 15 km in a three-dimensional model of the middle atmosphere. Gravity wave parameterizations are also starting to be incorporated into general circulation models to improve tropospheric simulations, specifically the tendency for high-resolution models to develop overly intense subpolar lows (e.g., Manabe et al., 1979) and excessively large jet stream velocities. Hansen et al. (1983) incorporated a Rayleigh friction-type parameterization in the lower stratosphere to simulate the effect of gravity-wave breaking, although the formulation was not associated with any specific tropospheric features. Gravity wave parameterizations associated with topography have been included in the new version of the British Meteorological Office (UKMO) general circulation model (GCM) (Palmer et al., 1986; Slingo and Pearson, 1986), as well as in the Canadian Climate Center (CCC) GCM (Boer et al., 1984). Attempts are now being made to quantify the influence of gravity waves generated in high-resolution (i.e., $1^\circ \times 1^\circ$, latitude by longitude) models, with indications that improvements can be obtained in the mesospheric simulation (Miyahara et al., 1986).

Gravity waves may exist at a variety of wavelengths; those of importance to the stratosphere and mesosphere have wavelengths on the order of 10–1000 km in the horizontal, and 1–100 km in the vertical in a static atmosphere, for such waves can propagate into the upper atmosphere without suffering excessive dissipation or reflection (Hines, 1960). Upper-atmosphere observations generally emphasize horizontal wavelengths of hundreds of kilometers, and vertical wavelengths of 1–20 km, although the more extreme ranges theoretically possible may not be determinable by the techniques available today (see the summary of Fritts, 1984). This wide variety of scales implies a wide variety in atmospheric processes responsible for gravity wave generation. The most favored mechanisms involve wave generation by convection (Pierce and Coroniti, 1966; Balachandran, 1980; Larsen et al., 1982), by wind shear (Balachandran and Donn, 1964; Keliher, 1975), and by flow over topography (Klemp and Lilly, 1978; Peltier and Clark, 1979). Geostrophic adjustment is a general process that will result in gravity wave generation (Blumen, 1972; Bosart and Cussen, 1973), but in practice it may be acting through convective and wind shear processes.

If gravity wave generation and breaking is responsible for the presumed dissipation in the stratosphere, it poses a severe test for global climate models. The suggested generation processes indicated above are in general not accurately simulated in general circulation models. The numerical schemes employed at several of the large-scale modeling groups do not accurately reproduce either the geostrophic adjustment process or flow over mountains, and the gravity waves that can be generated often have unrealistic numerical propagation characteristics (Arakawa and Lamb, 1977; Mesinger, 1982). In at least one instance, the horizontal resolution had to be reduced considerably below $1^\circ \times 1^\circ$ before the wind flow in the vicinity of the mountains matched observations (Dell'osso, 1984). Convection is a subgrid-scale parameterization in all GCMs; in some cases there is no actual calculation of mass flux. The vertical velocities associated with gravity wave generation are not calculated in the convection sub-routine. Furthermore, the hydrostatic assumption used to filter out high-frequency sound waves also removes high-frequency gravity waves, and will alter to some extent the nature of gravity wave breaking (Schoeberl, 1985a). The departure of these schemes from the actual process of convection (Frank, 1983) makes real gravity-wave generation unlikely. The accurate generation of gravity waves by shear instability requires high enough vertical resolution (perhaps on the order of a few hundred meters) to produce regions of Richardson number less than $\frac{1}{4}$, and even the subsequent propagation of the waves away from the generating region requires the proper vertical delineation of the background wind velocities. For global climate models, all of these problems are compounded by the much coarser

resolution that is employed, on the order of hundreds of kilometers horizontally, and several kilometers vertically.

Given these circumstances, one approach in developing a coupled climate/middle atmosphere model is to utilize a subgrid-scale parameterization for the gravity-wave-induced drag, similar in practice to the subgrid-scale approach used for convection. This paper describes the results of such a procedure with the GISS global climate model. Results are presented both with and without the parameterization to quantify its effects. In a companion paper (Rind et al., 1988) the model variability is discussed, emphasizing the complex interactions between the gravity wave drag, eddies, and the mean circulation. Comparisons with observations show to what extent this model is capable of simulating the middle atmosphere with coarse resolution and with a gravity wave parameterization consistent with current understanding of gravity wave phenomena.

2. Basic model descriptions

a. Global climate model

The model described here is an extended version of the global climate model of Hansen et al. (1983). It includes all the basic physics used in that model: numerical solution of the fundamental equations, heat and moisture transport through a two-layer ground, surface hydrological properties and albedo a function of vegetation type, complete radiative cloud calculations, diurnal cycle, etc. The primitive equations are solved on a grid-point domain of variable resolution; as of this time the extended climate simulations and the middle atmosphere model have been run with $8^\circ \times 10^\circ$ horizontal resolution.

The stratosphere and mesosphere are strongly influenced by processes originating in the troposphere (e.g., wave propagation, thermal radiation). Deficiencies in the tropospheric simulation will obviously limit the ability to simulate the middle atmosphere. (As a specific example, Mechoso et al., 1985, show how their forecast of a stratospheric warming is limited by the accuracy with which they can forecast the future position of the tropospheric jet stream, which influences the vertical propagation of planetary waves.) An extensive comparison of the tropospheric simulation has been made with observations (Hansen et al., 1983; Rind et al., 1984; Rind, 1986). The following are the primary deficiencies of the tropospheric simulations which may affect the middle atmosphere.

(i) Long-wave (wavenumbers 1–3) amplitudes are 30% deficient throughout the troposphere (Rind et al., 1984), and thus provide too small forcing at the base of the stratosphere. In conjunction, energy in wavenumbers 4–6 is too large by about 50% relative to that in wave numbers 1–3: the energy spectrum does not slope sufficiently (Rind, 1986). In addition, the synoptic-scale waves move too slowly.

(ii) The northward limit of the January Hadley Cell extends about 8° latitude (one grid box) too far north and the Ferrel Cell is too weak (Hansen et al., 1983; Rind, 1986).

(iii) The zonally averaged January jet stream is 15% too weak, as is eddy transport of angular momentum out of the jet stream (Rind, 1986).

(iv) The intertropical convergence zone and its movement are not properly simulated over some ocean areas (Hansen et al., 1983). One consequence is an excess of precipitation near 12°N during January (Rind, 1986).

Some of these deficiencies would be expected considering the coarse resolution of the model, and some of them are removed when the model is run with $4^\circ \times 5^\circ$ resolution (for example, synoptic-scale waves move faster, the Hadley Cell is more confined, energy in wavenumbers 4–6 decreases, jet stream increases, etc.). Finer resolution does not solve all problems; as noted earlier, models with increased resolution still have difficulty in reproducing proper long-wave characteristics (see also Hayashi and Golder, 1985, for a comparison of the GFDL 30 wave model with observations). Other aspects of the model need to be improved. Nevertheless, in its current state the coarse-grid model does well in certain respects: the eddy energy, energy transports, and ratio of transient to standing eddy energy all appear realistic (Hansen et al., 1983; Rind et al., 1984; Rind, 1986). The hemispheric energy cycle including baroclinic instability is of the proper magnitude (Rind, 1986), despite the model-resolvable scale being close to the limit for such transformations. Comparison of the model with this resolution to several other models with twice the resolution shows numerous similarities in performance (Schlesinger and Mitchell, 1985). Part of the reason for the model success on the coarse grid is the stability of the numerical scheme (Arakawa, 1972), and the use of the *B* grid with its enstrophy-conserving properties (Hansen et al., 1983; Sadourney, 1975), characteristics which allow the model to be run without any explicit diffusion. The model's eddy energy also benefits from a surface physics scheme which balances the surface drag and surface wind velocity (Hansen et al., 1983). On the basis of these comparisons we anticipate that this model will be useful for middle atmosphere simulations, although as we show, the deficiencies can affect the middle atmosphere model performance.

b. Climate-middle atmosphere model 1

The basic nine-layer model with a top at 10 mb was extended to 21 layers and the top was raised to 0.01 mb. This model was then used to simulate the troposphere and middle atmosphere. However, some additional changes were necessary in order for extended simulations to be made. A complete description of these

changes is given in Rind et al. (1984); here we simply review the major alterations.

Several changes were made to the numerical subroutine used in solving the fundamental equations. With no explicit dissipation in the middle atmosphere, winds near the model top accelerated to unrealistic values; thus a parameterized stability-dependent drag was added to the top three levels. The second-order scheme for advection of heat has a tendency to produce rather noisy patterns (Russell and Lerner, 1981); in the stratosphere the noise is not smoothed by convection and thus helps produce local wind gradients of large magnitude. To alleviate this problem, in the middle atmosphere the second-order differencing scheme for heat advection was replaced by the "slopes scheme", a higher-order upstream scheme which represents the distribution of the advected quantity (in this case potential temperature) within the grid box as a mean concentration and a slope. The scheme greatly reduces numerical noise and produces much smoother patterns (Russell and Lerner, 1981). Above 100 mb the model was altered to solve the fundamental equations in constant pressure coordinates to avoid spurious oscillations introduced by σ coordinates in regions of variable topography.

Additional refinements were also made in the radiation subroutine. The atmospheric ozone distribution, which is a key factor in determining the stratospheric temperature structure, was prescribed as a function of season, height and geographic location. The column abundances were taken from the monthly 10-year total ozone climatology compiled by London et al. (1976) at 10° latitude and 20° longitude intervals. The seasonal and latitudinal distribution of ozone above the 10 mb level was taken from London et al. (1977), based on Ogo 4 satellite observations, while below 10 mb we used the vertical profiles determined by Dutsch (1971, 1974). The ozone heating rates were obtained with the parameterization developed by Lacis and Hansen (1974). Although the option exists to retain the longitudinal variations in ozone concentration, only the zonal average values were used in the model runs. The shortwave radiation optical thicknesses for CO_2 , H_2O and O_2 were interpolated directly from numerical k -distribution tables instead of from analytic formulas (Hansen et al., 1983); the k -distribution is the probability density function such that $f(k)dk$ is the fraction of a specified frequency interval with absorption coefficient between k and $k + dk$ (Lacis and Hansen, 1974). Finally the thermal radiation absorption coefficients were refitted to obtain a more accurate integration over the zenith angle. The changes in the radiation code were made to improve its accuracy in rarefied regions.

With these changes the model was then run for 15 months, starting with real world initial atmospheric conditions from 1 December 1976. This will be referred to as "model 1"; except for the drag in the three top levels, it has no explicit momentum dissipation above

the tropopause. It is important to recognize the characteristics of this model without gravity wave drag to appreciate the effect of the parameterization described below.

The zonally averaged zonal wind and temperature for the second January (the 14th month of the simulation) are shown in Fig. 1. Comparison of these and other model results with observations (e.g., Figs. 2 and 10) reveals the following realistic features and discrepancies.

(i) The model successfully reproduces the overall stratospheric wind fields and their hemispheric differences. For example, the Southern Hemisphere winter stratospheric jet is of greater magnitude than that in Northern Hemisphere winter, with realistic values in

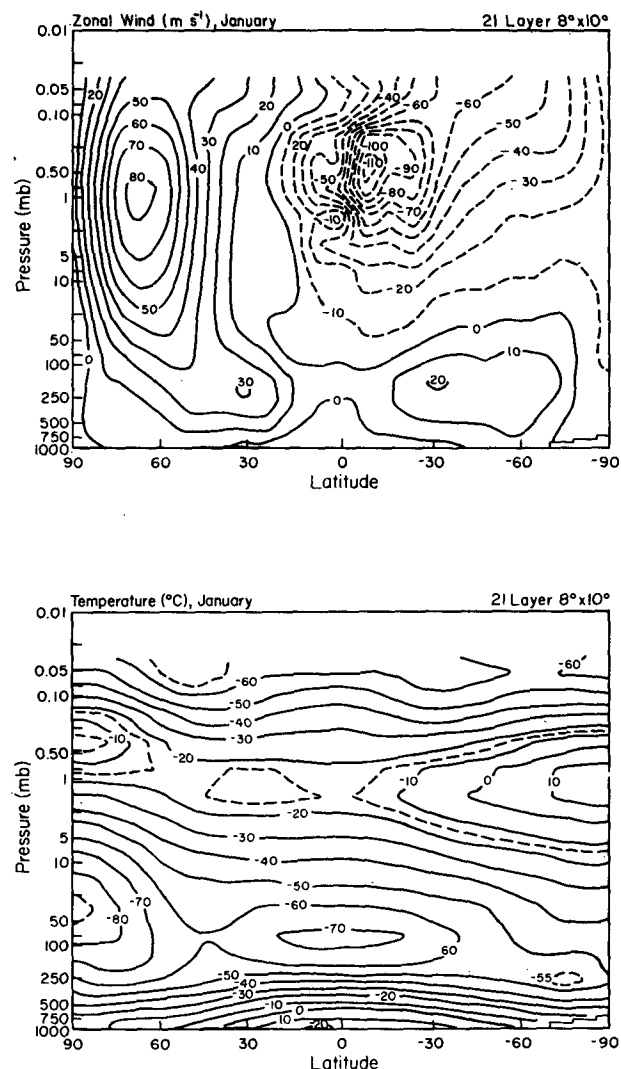


FIG. 1. Zonally averaged zonal wind (top) and temperature (bottom) for January, the 14th month run with model 1. Dashed lines indicate negative (east) winds, and intermediate temperature values. In this figure alone, the North Pole is on the left.

both cases (e.g., Newell, 1968; McGregor and Chapman, 1979). The jets also close off with altitude in a realistic manner, due to the parameterized drag included in the top three levels.

(ii) The low-latitude easterlies in the upper stratosphere cross over into the winter hemisphere. In this model the occurrence is related in part to the angular momentum divergence caused by the long waves in the winter hemisphere, as postulated by Hirota (1980), and is a realistic feature associated with the semiannual wind oscillation (see Rind et al., 1984 for a more complete description).

(iii) Low-latitude easterlies above 45 km are excessive, by about a factor of two. This deficiency has occurred in several other models, both three dimensional (3D) (e.g., Hunt, 1981) and two dimensional (2D) (e.g., Crane et al., 1980).

(iv) The model produces an apparent inertial oscillation near the equatorial stratopause (Rind et al., 1984).

(v) The vertical shear of the zonal wind to the north and above the tropospheric jet is too weak. This feature is also common to 3D models (Tenenbaum, 1982).

(vi) The seasonal and hemispheric stratospheric temperature differences are properly simulated, with the Southern Hemisphere colder in winter and warmer in summer (Labitzke, 1974; McGregor and Chapman, 1979). The colder winters are thought to be due to the reduced planetary wave activity in the Southern Hemisphere, while the warmer summers result at least partially from the shorter Earth-Sun distance during Southern Hemisphere summer. In the model there is a difference in solar radiation heating rates of $0.5\text{--}1^\circ\text{C day}^{-1}$ between the two hemispheres during summer.

(vii) The annual temperature cycle in the stratosphere appears to be realistic. In the Northern Hemisphere upper stratosphere, coldest temperatures occur in December, some warming occurs in January, followed by cooling again in February, before the onset of the spring warming in March. Warmest temperatures occur around the solstice in June. The lower stratosphere remains cold throughout the winter, as warming pulses which appear in the mid and upper stratosphere during January are less evident below 30 km. In the Southern Hemisphere upper stratosphere, coldest temperatures occur in the late fall, with gradual warming during the winter. In contrast, in the lower stratosphere coldest temperatures occur in midwinter. These features, and the hemispheric differences, have been observed from satellites (e.g., Labitzke, 1974, 1980, 1981; Labitzke and Barnett, 1973; Ghazi, 1976; McGregor and Chapman, 1979), from radiosonde data (e.g., Labitzke and Goretzki, 1982; Naujokat, 1981), and by rocketsondes (e.g., Groves, 1971; Koshelkov, 1977).

(viii) Model temperatures in the lower stratosphere during winter are too cold north of 60°N , by up to 10°C . This is consistent with the excessive zonal wind

in the lower stratosphere, and is a common model problem.

(ix) Temperatures in the upper mesosphere are not sufficiently cold in the summer hemisphere, and not warm enough in the winter hemisphere. Observations (Fig. 10) show temperature differences between the two hemispheres of 70°C (Barnett and Corney, 1985a), while the model results give differences of only 15°C . This implies that the summer to winter hemisphere meridional circulation cell in the upper mesosphere is not sufficiently intense.

(x) Upper-stratospheric long-wave amplitudes, especially that of wave 1, are generally excessively large. Peak amplitudes of 1000–2000 m occurred in five of the seven winter months in the Northern Hemisphere, in contrast to observations which show such an effect less than half the time (Geller et al., 1984).

The results presented here, as well as the detailed analysis given in Rind et al. (1984), indicate that the coarse-grid model is capable of producing a generally realistic simulation of stratospheric climatology, although deficiencies exist in the lower stratosphere and mesosphere. The model also produced a stratospheric warming during January, and certain aspects of the event were in accordance with observed characteristics of stratospheric warmings [e.g., downward propagation of wind and temperature changes, progression of the Aleutian High toward the pole, upward and poleward propagation of the Eliassen-Palm (EP) flux from the troposphere (Rind et al., 1984)]. The wave 1 geopotential height amplitude for this month peaked at a monthly average value of close to 2000 m, considerably larger than that found in the average January.

The model deficiencies occur in regions in which gravity wave-induced drag may be affecting the circulation in the real atmosphere. In order to improve the model simulation, we have included in the new version of the model ("model 2") parameterizations for gravity wave generation, propagation, breaking and associated drag on the model winds. In contrast to the gravity wave parameterizations which have been included in 2D models of the stratosphere (e.g., Holton, 1983), our parameterized gravity wave sources have a geographical distribution, and are associated with resolved model variables in the troposphere. The gravity wave effects will thus change as model values (and climate) change. In contrast to the gravity waves included in the UKMO and CCC climate models, the parameterized wave sources include convection and shear as well as topography, and affect the upper troposphere, stratosphere, and mesosphere. A description of the parameterization is given in the next section.

3. Gravity wave parameterization

The linear "saturation" theory of atmospheric gravity waves advanced by Lindzen (1981) and others has provided a scheme for parameterization of gravity wave

effects in global atmospheric models (e.g., Holton, 1982; 1983). According to the theory, the wave amplitude grows with height until convectively unstable regions are formed within the wave, resulting in the production of turbulence and just enough eddy diffusion to limit the wave amplitude to values corresponding to neutral static stability. The cessation of wave-amplitude growth with altitude results in the deposition of excess momentum and the acceleration of the background flow. The theory provides expressions for the acceleration of the background wind, and for the eddy diffusion coefficients due to this saturation process. The first step in applying this formulation is to estimate the momentum flux from each of the three gravity wave sources, and other wave parameters.

a. Parameterized gravity wave sources

The momentum flux associated with the parameterized gravity waves is made a function of three different processes in the model—flow over topography, convection, and wind shear. Values are calculated for each grid box in the model for each time step. The gravity wave characteristics for each source are defined as follows.

(i) *Topography*—Gravity waves associated with flow over regions of variable topography are assumed generated with a momentum flux proportional to the variance of the topography in each grid box following the formulation of Lindzen (1984):

MOMENTUM FLUX

$$F_m = \frac{1}{2} \rho_0 k V_0 \langle h^2 \rangle N_0 / (1 + l^2/k^2)^{1/2} \quad (1)$$

where $\langle h^2 \rangle$ is the variance of the topography calculated from the 1° resolution Scripps topography (Gates and Nelson, 1975), V_0 , ρ_0 , N_0 are the wind velocity, density and Brunt–Väisälä frequency averaged over the first two layers in the model (with a mean thickness of 800 m), respectively; k is the magnitude of the wavenumber vector, and has direction of the wind velocity; l is the wavenumber of a cosine envelope perpendicular to k , set equal to $1.1k$ as in Lindzen (1984). In practice it proved necessary to limit mountain wave generation to regions of relatively large topography variance ($\langle h^2 \rangle > 1.6 \times 10^5 \text{ m}^2$) as defined on the $8^\circ \times 10^\circ$ grid, to ensure that grid boxes with minimal topography were not generating mountain waves unrealistically. In addition, observations have shown that mountain wave generation is a nonlinear process (e.g., see the discussion of Pierrehumbert and Wyman, 1985, of results of the Alpine Experiment), not directly related to topography variance when topography is sufficiently steep. In recognition of this effect, an upper limit on the allowed topography variance is used, set equal to $2.025 \times 10^5 \text{ m}^2$, which for a 15 m s^{-1} surface wind and realistic Brunt–Väisälä frequencies gives a mountain wave momentum flux of 6 dyn cm^{-2} , in rough agree-

ment with maximum observed momentum fluxes (e.g., Lilly and Kennedy, 1973). The practice of limiting the maximum topography variance to similar magnitudes is employed by other modeling groups, (e.g., Palmer et al., 1986), and may be more consistent with apparent nonlinearities in the observed relationship. The specification of a limited range of allowable topography variance (of about 25%) implies that the topography variance primarily determines which grid boxes are allowed to generate mountain waves. Additional geographical variations in amplitude for the relevant grid boxes are associated with differences in wind velocity (which provide some dependence on the actual topography, as winds tend to be larger over higher terrain), as well as density and, from the ambient Brunt–Väisälä frequency, stability.

The wavenumber magnitude is calculated as a weighted average between a short wavelength (λ_2) determined by the minimum resolvable scale in the topography variance dataset and the largest wavelength defined by the size of the grid box (λ_1). We assume a weighting function ϵ inversely proportional to k , as shorter wavelengths will influence a more restricted portion of the grid box:

WAVENUMBER MAGNITUDE

$$k_m = \int_{k_1}^{k_2} (k \epsilon_k) dk / \int_{k_1}^{k_2} \epsilon_k dk \quad (2)$$

with $\lambda_2 = A^{1/2}$, where A is the area in a $1^\circ \times 1^\circ$ grid (the smallest length scale over which the topography variance is calculated), and $\lambda_1 = (\text{Area of grid box})^{1/2}$, the largest spatial scale for the topography variance. Note that the procedure does not include the topography variance or wavelengths on spatial scales above the Scorer wavelength (which generally varies between 10–50 km, e.g., Scoeberl, 1985a) but below the resolution of the topography dataset. In practice, the wave lengths vary between 80 km at the highest latitudes, and 270 km at low latitudes. These wavelengths are generally consistent with observations (e.g., Vincent and Reid, 1983).

We assume the mountain waves have zero phase velocity (ignoring nonlinear effects):

$$\text{PHASE VELOCITY } c_m = 0. \quad (3)$$

With this specification we are also ignoring traveling gravity waves associated with transient flow over topography.

The parameterized momentum flux is tested against saturation values and for critical levels, as described below, starting at the 583 mb level.

(ii) *Shear*—Shear generated gravity waves are parameterized with a momentum flux as estimated by Lindzen (1984):

$$\text{MOMENTUM FLUX } F_s = \rho_0 (\Delta V_0) |\Delta V_0| f / 240 N_0 \quad (4)$$

with ΔV_0 the wind shear between two successive layers and ρ_0 and N_0 representing the density and Brunt–

Väisälä frequency of the shear layer, with f the Coriolis parameter. Only one shear wave is calculated for each grid box. The calculation is begun at the jet stream level, and the wave propagation is examined through the stratosphere. If the wave hits a critical level below 60 km its influence would be minimal, due to the small magnitude of the shear wave momentum flux, and thus it is ignored. Instead, a new wave is generated at the critical level, and its propagation is examined up to 60 km. This procedure is repeated until a wave is found which will propagate through the 60 km level; otherwise the shear at 60 km is used to generate the wave.

The wavenumber is oriented in the direction of the wind shear, and the wave length is set equal to the value calculated for mountain waves,

$$\text{WAVENUMBER MAGNITUDE } k_s = k_m. \quad (5)$$

The phase velocity is set equal to the average wind velocity in the shear layers, projected in the direction of the shear:

$$\text{PHASE VELOCITY } c_s = [(V_1 + V_2)/2] \cdot \Delta V / |\Delta V|. \quad (6)$$

(iii) *Convection*—Convective generated gravity waves are parameterized with a momentum flux proportional to the vertically integrated convective mass flux squared, in a general form similar to that in (1) for topography:

MOMENTUM FLUX

$$F_c = (\text{constant}) \rho_0 k (MF^2)^2 N_0 V / |V| \quad (7)$$

where MF is the vertically integrated mass flux over the convective region, ρ_0 and N_0 are the density and Brunt–Väisälä frequency at the top of the convective region, and V is the wind velocity averaged over the convective layers. The wavenumber is oriented in the direction of this wind, with a magnitude equal to that for mountain waves,

$$\text{WAVENUMBER MAGNITUDE } k_c = k_m. \quad (8)$$

The phase velocity is set equal to the mean wind over the convective region $\pm 10 \text{ m s}^{-1}$,

$$\text{PHASE VELOCITY } c_c = |V| \pm 10 \text{ m s}^{-1}. \quad (9)$$

In addition, when penetrating convection occurs (i.e., when the mass flux penetrates the 400 mb level), two additional phase velocities are added: $c_c = |V| \pm 20 \text{ m s}^{-1}$, and $c_c = |V| \pm 40 \text{ m s}^{-1}$. As shown in section 4e, and in Holton (1983), the use of higher phase-velocity gravity waves improves middle atmosphere simulations. Observations continually indicate waves with as high, or higher phase velocities in the mesosphere (e.g., Meek et al., 1985; Yamamoto et al., 1986), similar phase velocities have been used in simpler middle atmosphere models (e.g., Matsuno, 1982), and such high-phase velocities have been found in the high-resolution GFDL middle-atmosphere simulation (Miya-

hara et al., 1986). But are such waves ever associated with penetrating convection? While there is no empirical evidence as of yet, certain aspects of convective events suggest that possibility. Internal gravity wave phase velocities maximize under conditions of high wind velocities in the shear layer (e.g., Bedard et al., 1986); deep tropical convection is associated with strong gust fronts (Lipps and Hemler, 1986), and severe thunderstorms are apparently associated with a large spread of radial velocities (e.g., Istok and Doviak, 1986). As coarse-grid general circulation models cannot resolve the severe winds associated with localized convection, the use of the increased spread of phase velocities around the mean grid box wind value is an attempt to incorporate their impact on gravity wave generation.

b. Gravity wave induced drag and diffusion

Gravity waves propagate in the vertical with constant momentum flux until this momentum flux exceeds the saturated value defined by the background wind and temperature profile (Lindzen, 1984; Holton, 1982; Fritts, 1984):

$$F_{\text{sat}} = \rho k (\hat{\mathbf{k}} \cdot \mathbf{V} - c)^3 / 2N(1 + l^2/k^2)^{3/2}. \quad (10)$$

At critical levels, F_{sat} is zero, and the wave totally dissipates in that layer. In the model, once the parameterized waves are formed, their momentum fluxes are compared to F_{sat} between the generating source and the model top. The mountain waves redistribute momentum starting at the 583 mb level, as their relatively large momentum fluxes can affect upper-tropospheric processes. Shear and convective waves are ignored in the troposphere, with the exception that their momentum flux cannot exceed the saturated value. Above the tropopause ($\sim 100 \text{ mb}$), the waves' progress is continually checked for momentum flux in excess of saturation, and any excess is deposited.

In addition to the effects of saturation and critical levels on the wave, radiative damping is also evaluated. The vertical group velocity is calculated as

VERTICAL GROUP VELOCITY

$$G_w = (\hat{\mathbf{k}} \cdot \mathbf{V} - c)^2 k / N, \quad (11)$$

using the values of V and N in each layer, and the phase velocity for each wave. The transit time is then calculated as

$$\text{TRANSIT TIME } t = \Delta z / G_w \quad (12)$$

for the thickness Δz of each layer. The transit time is compared to the radiative time constant as estimated by Fels (1982):

RADIATIVE TIME CONSTANT

$$\tau = (960/T)^2 e^{-960/T} f(m, z) \quad (13)$$

with $f(m, z) = a(z) + b(z)m^2/(c(z) + m^{3/2})$ and the

coefficients $a(z)$, $b(z)$ and $c(z)$ as derived in Fels (1982) [note: $b(z)$ as printed in that text is incorrect, the first minus sign inside the square root in Eq. (22b) should be plus]. The momentum flux F of a wave, incident on the base of a layer, is reduced by $e^{-2l/\tau}$ as it passes through, and this radiative drag is deposited in the layer,

RADIATIVE DAMPING

$$V_{\text{RAD}} = [1/(\rho\Delta Z)]Fe^{-2l/\tau}. \quad (14)$$

The remaining flux is compared with F_{sat} at the top of the layer, and, if greater, is reduced to F_{sat} , again accelerating the local wind. The total drag on the wind is thus calculated as

WAVE DRAG

$$V_{\text{DRAG}} = \frac{1}{\rho\Delta Z} (F(1 - e^{-2l/\tau}) - F_{\text{sat}}). \quad (15)$$

In case the initial flux F was already saturated, the wave drag is equivalent (for purely zonal flow) to the usual expression (e.g., Lindzen, 1981)

$$U_t = -k(U - c)^2 \{ [(U - c)/H] - 3U_z \} / 2N(1 + l^2/k^2)^{3/2}. \quad (16)$$

Note that the gravity wave absorption can actually increase the wind, depending on the relationship between U and c .

The wave breaking is assumed to generate turbulent diffusion in the vertical, limiting the amplitude so that the wave remains just saturated. The eddy diffusion coefficient due to this process is related to the wave drag (Lindzen, 1981) as

$$D = \frac{1}{\rho\Delta Z} V_{\text{DRAG}} \cdot (V - kc)/N^2 \quad (17)$$

and the diffusion then changes the zonal wind profile,

$$\rho V_{\text{DIF}} = (\rho 2DV_z)_z \quad (18)$$

(doubling the diffusion on the wind field, and thus omitting its effect on the thermal field, as suggested by Chou and Schoeberl, 1984).

The momentum flux budget is balanced—momentum flux generated at the source is equal to the total flux convergence by radiative damping and wave drag. In practice, the momentum flux that would have exited the top model layer is absorbed in that level (approximately 85 km), which increases the drag in the layer by about 30%.

To conserve energy, the kinetic energy lost is put back into the model in the form of heat, as

$$\frac{1}{2} \rho \Delta(V^2) = \rho c_p \Delta T. \quad (19)$$

Finally, to allow the dynamics to more fully adjust to the drag, the parameterization is incorporated into the numerical solution of the momentum equation, and calculated 8 times every hour. The effects of this

parameterization on the multilayer run of the new model are discussed in the next section.

4. Model-2 results

The parameterized gravity-wave drag was incorporated into the model 1 version of the climate-middle atmosphere model, and the model top was raised to 0.0022 mb (approximately 87 km) with the addition of two more vertical layers. Several other changes were also implemented, associated with the radiation scheme. Comparison of the model CO₂ longwave radiation with line by line calculations indicated that the absorption coefficient needed to be reduced by 20% in the upper stratosphere/lower mesosphere. Furthermore, in model 1, tropospheric water vapor gradually accumulated in the stratosphere and led to anomalous cooling. It was thus decided to use a specified water vapor amount in the stratosphere and mesosphere of $3 \times 10^{-6} \text{ g g}^{-1}$ rather than the calculated model values.

The model-2 version of the GCMAM was run for five years, following a spin up of ten months done with model 1. During the first two years the Coriolis force and metric term were set to zero at the pole, as in the standard UCLA model code (Arakawa, 1972); during the last three years the full value for these terms was used, as in the nine-layer GISS model 2 (Hansen et al., 1983). The difference between these formulations affects the circulation only near the pole (Hansen et al., 1983). In recognition of this difference, the zonal wind standard deviations calculated for the latitude closest to the pole in each hemisphere will be for the last three years. Unless otherwise stated, all other model results will be for the five-year average.

A brief description of the different physical processes included in this model is presented in Table 1. With the exception of the changes in the numerical scheme and radiation code discussed above, they are identical to those used in the nine-layer model. The vertical layering for the primary grid variables (temperature, horizontal wind, height and humidity) is shown in Table 2, with the vertical wind and vertical transports calculated at the layer interfaces. The table also lists the global average geometric altitude associated with the pressure values in the model. For the presentation of the figures, the model results in pressure coordinates are transformed to height coordinates using the relationship

$$z = -7.0 \ln(p/p_s) \quad (20)$$

where $p_s = 984 \text{ mb}$. This equation produces the “approximate” altitudes shown in the right-hand column of Table 2, which differ from the true altitude by 2% at most.

a. Zonal wind

The model-generated zonal winds as a function of latitude and altitude are shown in Fig. 2 for Dec–Feb and June–Aug, along with observed values (calculated in the extratropics from the geostrophic wind relation-

TABLE 1. Global climate/middle atmosphere model characteristics.

Model resolution	$8^{\circ} \times 10^{\circ}$, 23 layers, 0.001 mb top
Numerical scheme	Primitive equations, <i>B</i> -grid, energy (enstrophy) conserving, second order, slopes scheme for heat above 100 mb, σ coordinates in troposphere, p coordinates above 100 mb, leap-frog time step, high-latitude Fourier filter, Shapiro filter for sea level pressure, parameterized gravity wave drag from mountains, shear, and convection.
Radiation	Short wave by single Gaussian point method, long wave by correlated- k ; includes standard gases plus N_2O , CH_4 , O_3 , and NO .
Topography	Topography averaged from $1^{\circ} \times 1^{\circ}$; fractional grid for land, water, sea ice, land ice.
Surface properties	Surface albedo varies geographically and seasonally with 8 prescribed vegetation types, albedo wavelength dependent, snow albedo a function of snow depth, age, vegetation type, ocean albedo a function of solar zenith angle and wind speed, emissivity a function of wavelength for desert, snow, ice and ocean.
Ground and surface	Two-layer soil, heat conduction equation, simultaneous calculation of surface wind, temperature and drag, evapotranspiration a function of vegetation type and season, water holding capacity a function of vegetation.
Surface fluxes	Monin-Obukhov theory for drag coefficient, surface roughness a function of topography variance and vegetation type, and wind speed squared over ocean.
Boundary layer	Height determined by dry convection.
Convection	Penetrating convection due to moist static instability, $\frac{1}{2}$ grid box rising, momentum mixing.
Cloud cover	Determined by relative humidity and extrapolated subgrid-scale temperature variance, albedo and absorption vary with cloud height.

ship). Successful features of the simulation include the proper break between the tropospheric and stratospheric jets, realistic differences between winter and summer in each hemisphere, and interhemispheric differences, such as the stronger winter stratospheric jet in the Southern Hemisphere. Even the downward slope of the summer easterlies from high to low latitudes is evident. Comparison with Fig. 1 shows that the outstanding problems in the zonal wind field of model 1 have been alleviated.

The seasonal variation of the zonal winds at several different pressure levels is examined in Fig. 3. Com-

parison of the observed and modeled winds in the lower stratosphere (Fig. 3 top) shows that the model is successfully reproducing the reduced winter westerlies in the Northern Hemisphere where many models have been most deficient (e.g., Tenenbaum, 1982). Note also that in both the model and observations, the lower-stratosphere winter westerlies are of greater magnitude in the Southern Hemisphere; as shown below, in the model this difference is at least partly the result of the difference in topography and mountain wave drag between the hemispheres.

In the upper stratosphere (Fig. 3, middle) both model results and observations show similar seasonal variations in the extratropics. In the Northern Hemisphere, the largest zonal wind values are found in the early winter, followed by reduced values in January, and a return to somewhat stronger winds in February. This is due to the occurrence of warmings which reduce the zonal kinetic energy during midwinter. In the Southern Hemisphere the strongest winds are found in early winter, with a decrease throughout the remainder of the season (e.g., Labitzke, 1981). As discussed earlier, this feature was present in model 1 as well. Model late-winter zonal winds appear to be somewhat stronger in both hemispheres than is observed, implying a delay in the final spring warming, although there is much interannual variability in the Northern Hemisphere. The midstratosphere summer easterlies are of the appropriate magnitude, although model peak values may be shifted somewhat equatorward. The observed semi-annual oscillation in the tropics, with easterly winds at the solstices and west winds during the equinoxes, is also evident in the model.

The model zonal winds in the mesosphere appear to have the proper seasonal and latitudinal variation, and even the times of the spring warming appear reasonable (Fig. 3, bottom). The model west winds are somewhat weaker than observed, although the geostrophic wind approximation used to derive the observed winds may be inadequate above 60 km because

TABLE 2. Model layering for primary variables.

Level	Pressure (mb)	Height (km)	Approximate height (km)
* Radiation only	0.000	104.4	*
* Radiation only	0.001	94.4	*
* Radiation only	0.002	89.0	*
23	0.004	84.7	86.892
22	0.007	81.0	82.974
21	0.015	77.1	77.639
20	0.032	72.4	72.336
19	0.068	67.5	67.059
18	0.147	62.3	61.663
17	0.316	56.8	56.305
16	0.681	51.0	50.931
15	1.5	45.1	45.403
14	3.2	39.3	40.099
13	6.8	33.7	34.823
12	14.7	28.5	29.426
11	31.6	23.5	24.069
10	68.1	18.7	18.695
9	149.3	13.7	13.200
8	272.3	9.9	8.993
7	424.3	6.8	5.888
6	583.9	4.3	3.653
5	729.6	2.5	2.094
4	840.1	1.4	1.107
3	906.5	0.8	0.574
2	944.9	0.5	0.284
1	972.1	0.3	0.085

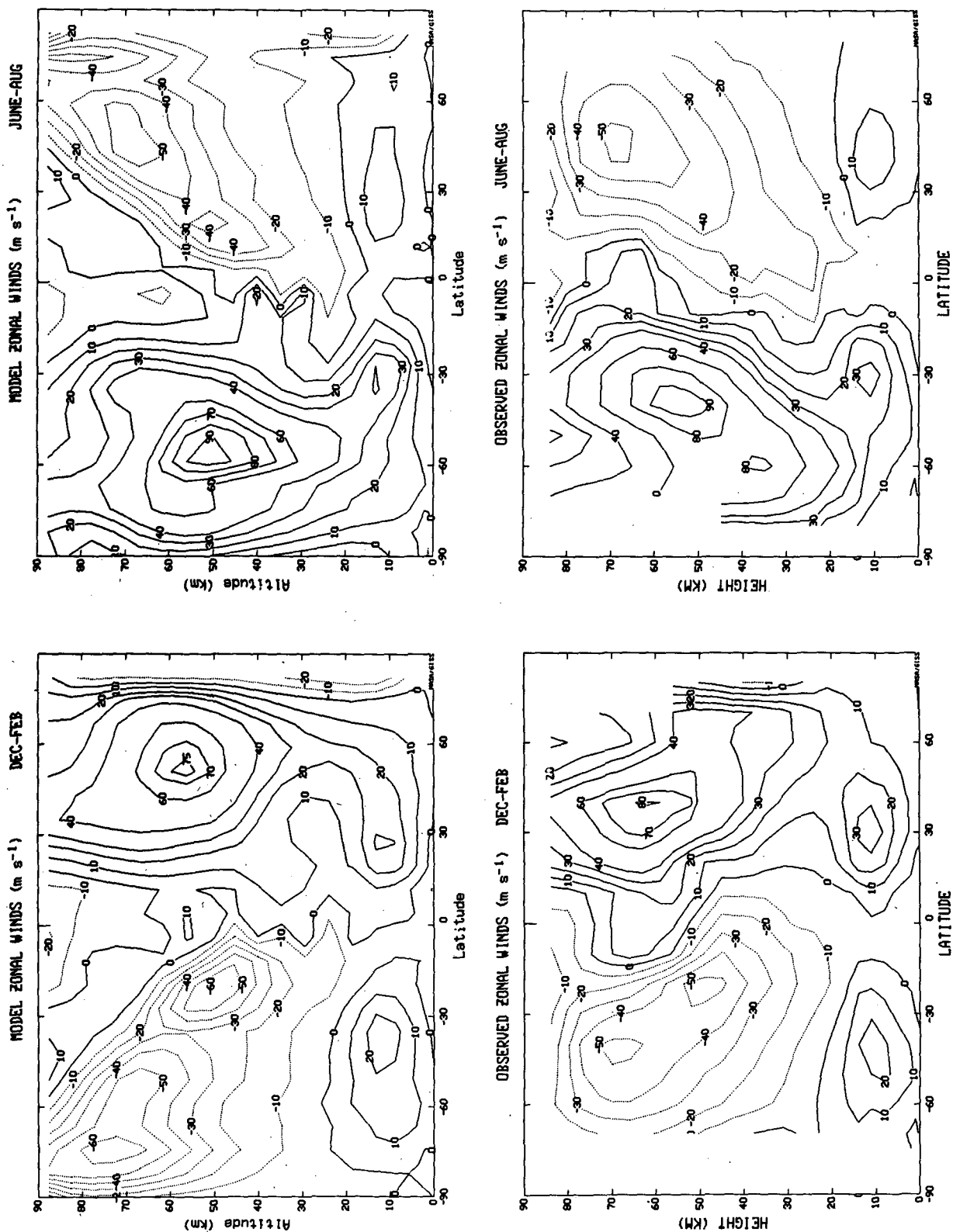


FIG. 2. The GCMAM model 2 (top) and observed (bottom) zonal winds for Dec-Feb (left) and Jun-Aug (right). Model results in this and other figures are from 5-year averages, unless otherwise stated. Observations are the geostrophic wind estimates from Barnett and Corney (1985a) from 20°–70° latitude in each hemisphere, and rocket and balloon observations in the tropics (Groves, 1971).

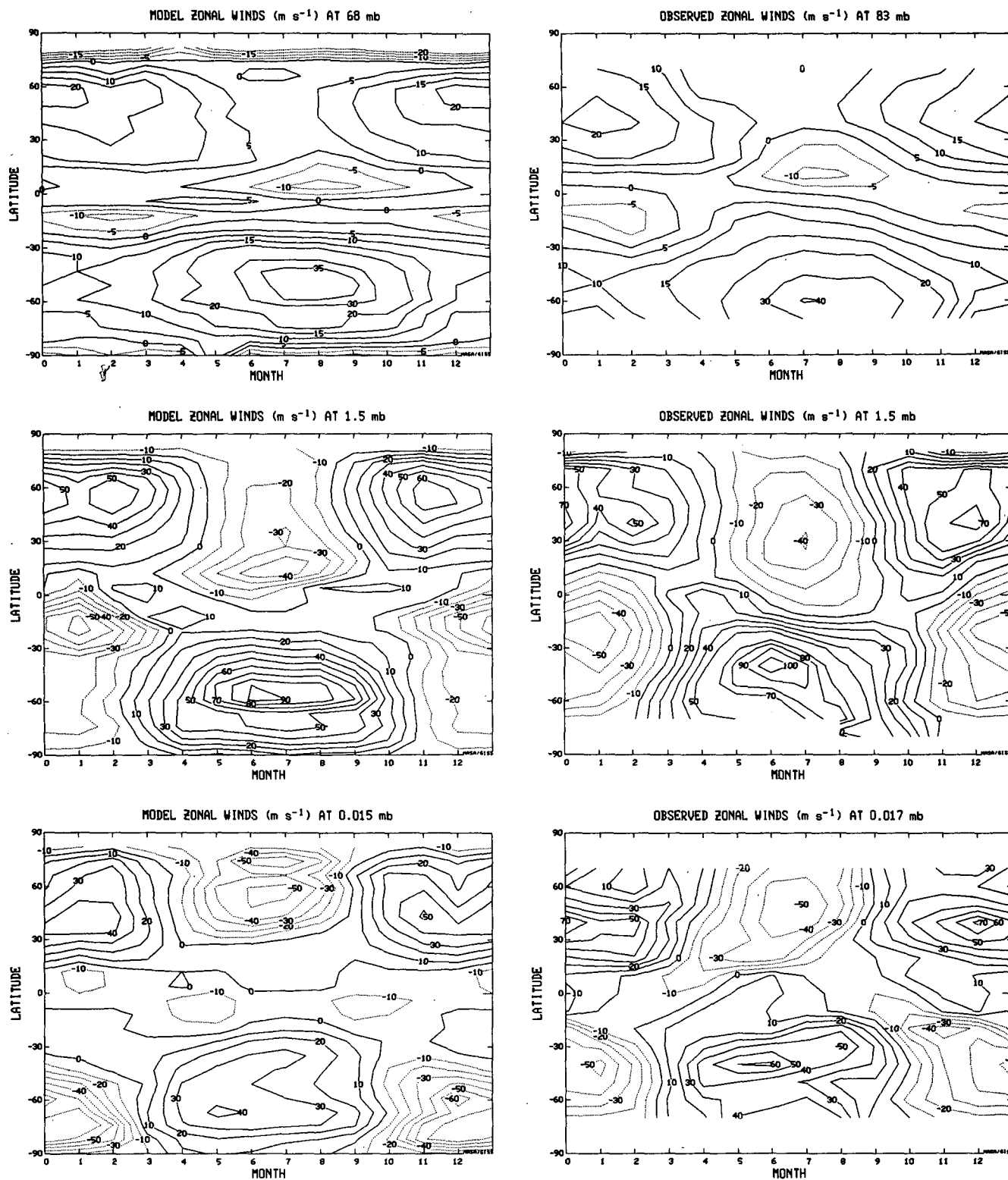


FIG. 3. Latitudinal average zonal winds versus month (January is month 1) from the model (left) for 68, 1.5, and 0.015 mb (top to bottom), and from observations (right) for 83, 1.5 and 0.017 mb. Observations from the sources listed for Fig. 2.

of forcing by tides and gravity waves (Barnett and Corney, 1985a).

The change with time of the zonally averaged zonal winds can be written in terms of the transformed mean zonal momentum equation (e.g., Andrews and McIntyre, 1978):

$$\frac{\delta(\bar{U})}{\delta t} = -\left\{\frac{\delta(\bar{U} \cos \phi)}{a \cos \phi \delta \phi} - f\right\} \bar{v}^* - \frac{\delta \bar{U}}{\delta p} \bar{\omega}^* + \frac{1}{a \cos \phi} (\nabla \cdot \mathbf{F}) + \bar{X}, \quad (22)$$

where the transformed circulation v^* , ω^* is defined as

$$\begin{aligned} \bar{v}^* &= \bar{v} - \frac{\delta\{(v'\bar{\theta}')/(\delta\bar{\theta}/\delta p)\}}{\delta p}; \\ \bar{\omega}^* &= \bar{\omega} + \frac{\delta\{(v'\bar{\theta}') \cos \phi/(\delta\bar{\theta}/\delta p)\}}{a \cos \phi \delta \phi}. \end{aligned} \quad (23)$$

The Eliassen-Palm (EP) flux divergence ($\nabla \cdot \mathbf{F}$) is

$$\begin{aligned} \nabla \cdot \mathbf{F} &= \frac{\delta(F_{(\phi)} \cos \phi)}{a \cos \phi \delta \phi} + \frac{\delta(F_{(p)})}{\delta p}; \\ F &= \{F_{(\phi)}, F_{(p)}\} = a \cos \phi \left\{ -\bar{u}'v' + \frac{\delta \bar{U}}{\delta p} \frac{\bar{v}'\bar{\theta}'}{\delta \bar{\theta}/\delta p} \right. \\ &\quad \left. - \bar{u}'\bar{\omega}' - \frac{\bar{v}'\bar{\theta}'}{\delta \bar{\theta}/\delta p} \left(\frac{\delta \bar{U} \cos \phi}{a \cos \phi \delta \phi} - f \right) \right\} \end{aligned} \quad (24)$$

and \bar{X} is any mean nonconservative force, in this case the drag (Dr) due to the different parameterized gravity wave sources and the associated vertical diffusion (Dif)

$$\bar{X} = (\overline{\text{Dr}} + \overline{\text{Dif}}) \{ \text{Mtn, shear, moist convective} \\ |V| \pm 10, 20, 40 \}. \quad (25)$$

The total change with time over the winter and summer seasons is relatively small, so an approximate balance exists among the change due to the transformed stream function, the eddy EP flux divergence, and the gravity-wave-induced drag. The different components of this balance are shown in Figs. 4–7, and the geographical distribution of the gravity wave sources are presented in Figs. 8 and 9. (Note that while these figures show the effect of the gravity wave parameterization on the zonal wind, the drag and diffusion act on the total wind vector.) The basic balance in most regions of the winter troposphere and stratosphere is between the westerly acceleration of the transformed stream function and the deceleration induced by eddies and by gravity wave drag. The transformed streamfunction represents, to some extent, the diabatically driven streamfunction (e.g., Dunkerton, 1978) as well as the circulation generated by the gravity-wave-induced drag [although as emphasized by Hitchman (personal communication) the diabatic circulation may be regarded as due, in part, to gravity wave absorption, an irreversible, nonadiabatic process]. The transformed streamfunction is characterized by equator to pole flow

in the troposphere and lower stratosphere, and flow from the summer to winter hemisphere in the mesosphere. When acted upon by the Coriolis force this produces westerly accelerations throughout the winter atmosphere, with easterly accelerations in the summer mesosphere and small westerly acceleration below (Fig. 4, top). The model meridional velocities (both \bar{v} and v^*) range from 5 to 15 m s⁻¹ in the mesosphere, in agreement with both estimated (Gartner and Memmesheimer, 1984) and observed (Gregory et al., 1981) magnitudes.

The EP flux convergences are due to transience, or nonconservative effects such as radiative damping, gravity-wave-induced drag or critical line absorption (for stationary eddy energy, critical lines of zero wind velocity reside at low latitudes). The different effects are apparent in the model (Fig. 4, bottom) with EP flux convergences providing easterly accelerations at low latitudes, especially in the Northern Hemisphere winter, as well as winter decelerations in regions with gravity wave drag and transience. As will be shown below, the eddy heat and momentum transports which comprise the EP flux are in agreement with observations in the upper stratosphere and mesosphere, although they may be 25% too small in the low and mid-stratosphere. The tropical easterly portion of the semi-annual oscillation appears in this model to be the result of both mean circulation and eddy effects at least in the winter hemisphere, in agreement with the suggestion of Hopkins (1975) and Hirota (1980), as well as the GFDL SKI-HI model results reported by Mahlman and Umscheid (1984). The equatorial westerlies during the equinox are also forced by both mean circulation and eddy effects, with eddy E-P flux divergences possibly associated with model-resolved Kelvin waves (Rind et al., 1984). The Kelvin waves in the model superficially resembled the observed (Wallace and Kousky, 1968; Hirota, 1980), with eastward-traveling oscillations in the zonal wind field of 15–30 day period in the lower stratosphere, 10–20 day period in the mid-stratosphere, and substantial energy in periods as short as 5–10 days in the upper stratosphere. The change in period as a function of altitude is expected, as the damping rate of Newtonian cooling increases with decreasing Doppler-shifted frequency (Holton, 1975).

Hitchman (personal communication) suggested that the tropical EP flux divergences might be the result of longitudinally varying inertial circulations. This model does produce inertial oscillations (as was true for model 1), which vary with longitude above 1 mb. The oscillations do not appear in the zonal wind climatology shown in Fig. 2 due to the monthly variability of the effect; it will be more apparent in the discussion of model variability, in part II of the presentation of model results (Rind et al., 1988).

Geller et al. (1983, 1984) and Hartmann et al. (1984) report the presence of high-latitude regions of positive EP flux divergence during winter in both hemispheres.

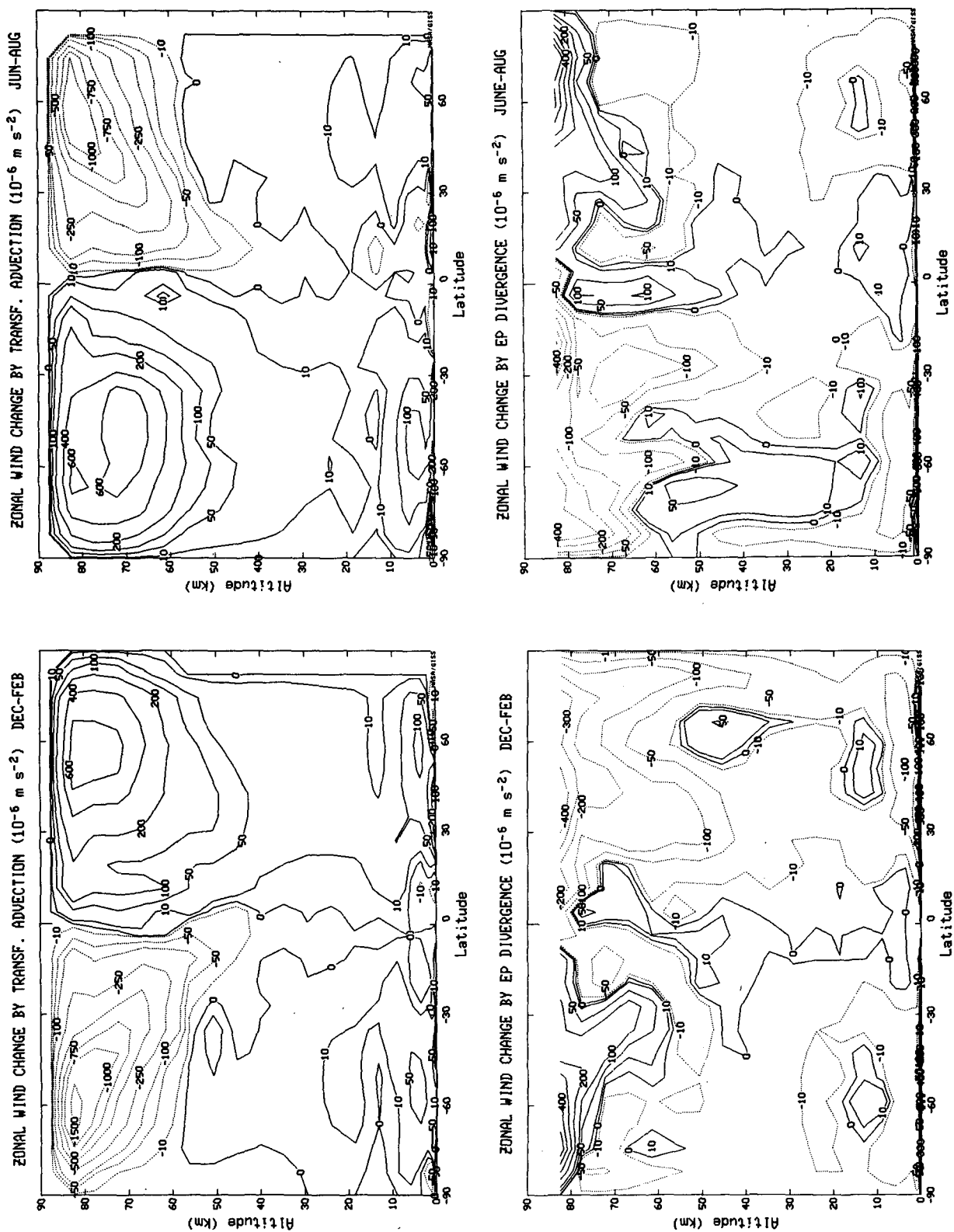


FIG. 4. Model zonal wind change by transformed advection (top) and EP flux divergence (bottom) for Dec-Feb (left) and Jun-Aug (right).

Robinson (1986) raised the question of whether this result was not an artifact of representing the actual EP flux by its geostrophic counterpart, due to an overestimation of the eddy-momentum flux divergence at high latitudes produced by using geostrophic winds. The model results in Fig. 4 were calculated with the full primitive equation terms (equation 24) and the actual model winds. The model produces two regions of EP flux divergence in the middle atmosphere of the winter hemispheres. During Northern Hemisphere winter the major region is located in the vicinity of the stratospheric jet, while there is a smaller more variable region poleward of the jet in the middle to upper stratosphere (which is sufficiently variable from month to month that it is not obvious on the seasonal average). In the Southern Hemisphere the major region is poleward of the jet, with a more variable region equatorward. In both hemispheres the poleward regions are associated with negative meridional gradients of potential vorticity and so diabatic effects or dissipation may be acting to generate wave activity. We show below (Table 4b) that this is a distinct possibility. However, the more equatorward regions are not associated with reversed potential vorticity gradients (at least on the monthly average) and so may actually imply an in situ source of wave activity, although given the zonal asymmetry in the inertial oscillation in the lower mesosphere, they may represent local changes in the sign of the gradient not apparent on the zonal average. Note that as these results represent seasonal averages they are unlikely to be associated with wave-transient decay. Boville (1985) found regions of monthly EP flux divergence using the full primitive equation form in some general circulation model experiments with the NCAR community climate model (CCM).

The parameterized gravity-wave-induced drag due to topography is the only momentum drag mechanism in the model to affect the lower stratosphere. It acts to decelerate the west winds (Fig. 5, top), and is responsible for the ability of this version of the GCMAM to produce a realistic separation of the tropospheric and stratospheric jets (compare Figs. 1 and 2). Due to the difference in topography between hemispheres (Fig. 8, top), this mountain drag is less effective at Southern Hemisphere midlatitudes, and so the lower stratospheric westerlies are stronger there (Fig. 2, 3); when the mountain drag is removed, there is little difference in the model in the west wind strength at 68 mb between the winter hemispheres. The mountain drag is also an effective decelerating agent in the upper stratosphere, with magnitudes approaching that of the EP flux divergence. The mountain-wave momentum fluxes impinging upon the upper troposphere are on the order of those observed (e.g., Lilly and Kennedy, 1973). Note also the maximum influence of these waves in the stratosphere is during winter (due to the seasonal variation in source strength), in agreement with the observations (for all gravity waves) discussed, for example, by Hirota (1984).

The parameterized shear-generated gravity waves are several orders of magnitude smaller than the mountain waves (Fig. 8, middle) and therefore break at higher altitudes. They are responsible for decelerating the mesospheric westerlies in the winter hemisphere and the mesospheric easterlies in the summer hemisphere, zonal winds which are being accelerated by the effect of the Coriolis force on the transformed meridional winds (Fig. 4). The shear-wave sources occur in the vicinity of the tropospheric jet streams (Fig. 8, middle), but not necessarily in the regions where the tropospheric jet is strongest. Shear-generated gravity waves produced in the troposphere often encounter critical levels in the lower stratosphere, so the locations of the shear-wave sources which affect the mesosphere may be very different from those which produce gravity waves observed at the surface (e.g., Balachandran and Donn, 1964). Monthly peak phase velocities associated with the shear waves are $20\text{--}25\text{ m s}^{-1}$ (Fig. 8, bottom).

The parameterized moist convective gravity waves are of magnitudes similar to those for the shear waves, and thus also primarily affect the mesosphere (Fig. 6). The convectively generated waves with $c = V \pm 10\text{ m s}^{-1}$ are associated with any type of moist convection and so occur both in regions of tropical or summertime convection, and also in storm track locations (which are known to be convective) (Fig. 9, top). In the model, these waves act along with the shear drag to balance the easterly acceleration of the transformed advection in the summer extratropical mesosphere (plus the effects of the gravity wave-induced diffusion); in the winter hemisphere their effect is the same order of magnitude as that of both the shear drag and the EP flux convergence which, together, balance the westerly acceleration of the transformed mean circulation and gravity wave diffusion.

The sources for the convectively generated waves with $c = V \pm 40\text{ m s}^{-1}$ are the penetrating convection regions that occur primarily at low latitudes. Their effect is mainly to balance the transformed advection accelerations in the tropics and subtropics, especially in the summer hemisphere; note that the gravity wave sources with smaller phase velocities (both $c = V \pm 10\text{ m s}^{-1}$, and $c = V \pm 20\text{ m s}^{-1}$) encounter critical levels prior to reaching the mesosphere and are thus ineffective in providing the necessary drag.

The total wave drag provided by the different mechanisms is close to the value of $100\text{ m s}^{-1}/\text{day}$, generally thought to be necessary, and used in middle atmosphere models (e.g., Holton, 1983). The decelerations in the winter mesosphere are of the same order of magnitude as those calculated by Miyahara et al. (1986) in the GFDL high-resolution model due to gravity wave drag, but they are about five times greater than the GFDL results in the summer mesosphere. As noted by Miyahara et al. (1986) their model produced excessive mesospheric easterlies in the summer hemisphere.

The wave breaking is accompanied by vertical diffusion [eqs. (17, 18)], which acts to smooth out the

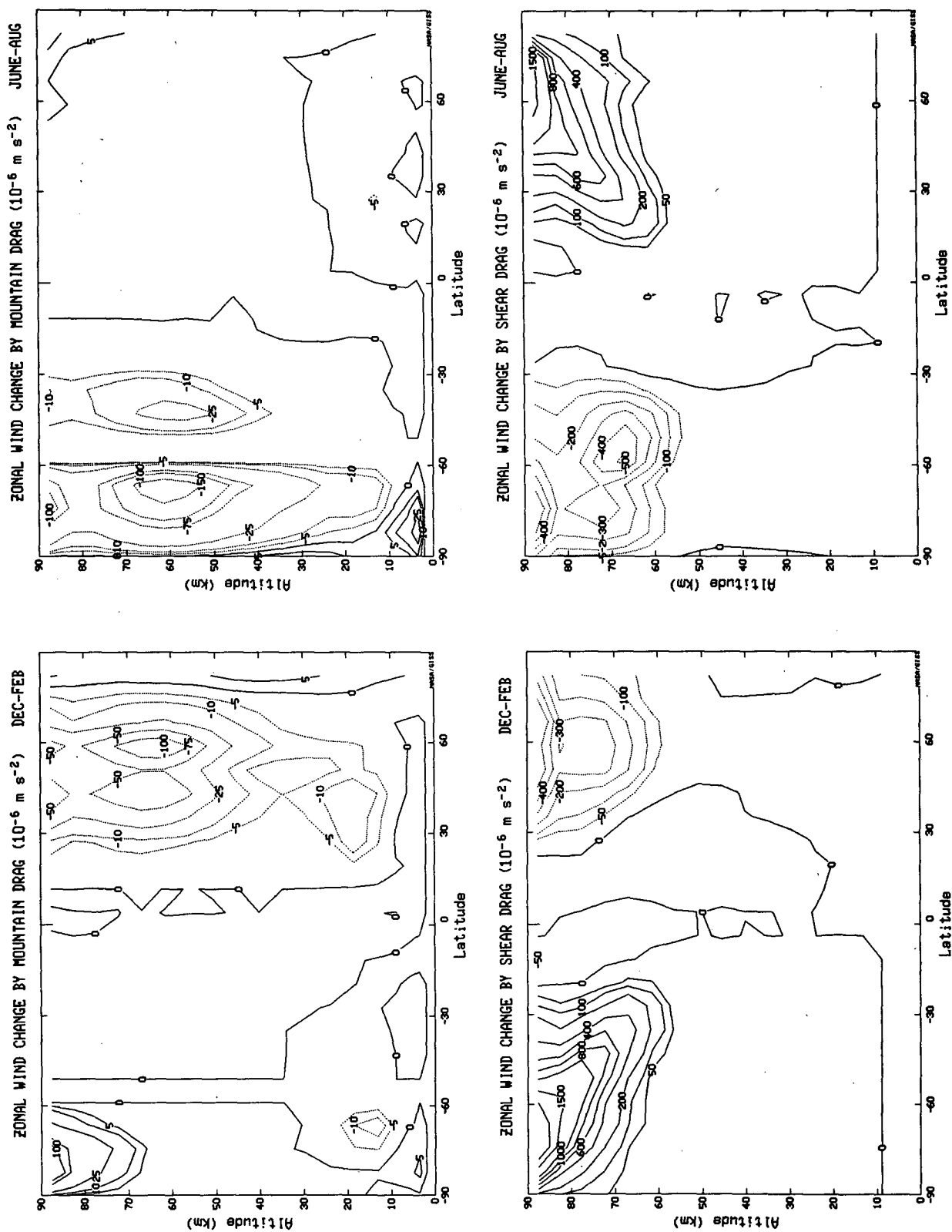


FIG. 5. As in Fig. 4 but for drag due to parameterized gravity waves from topography (top) and shear (bottom).

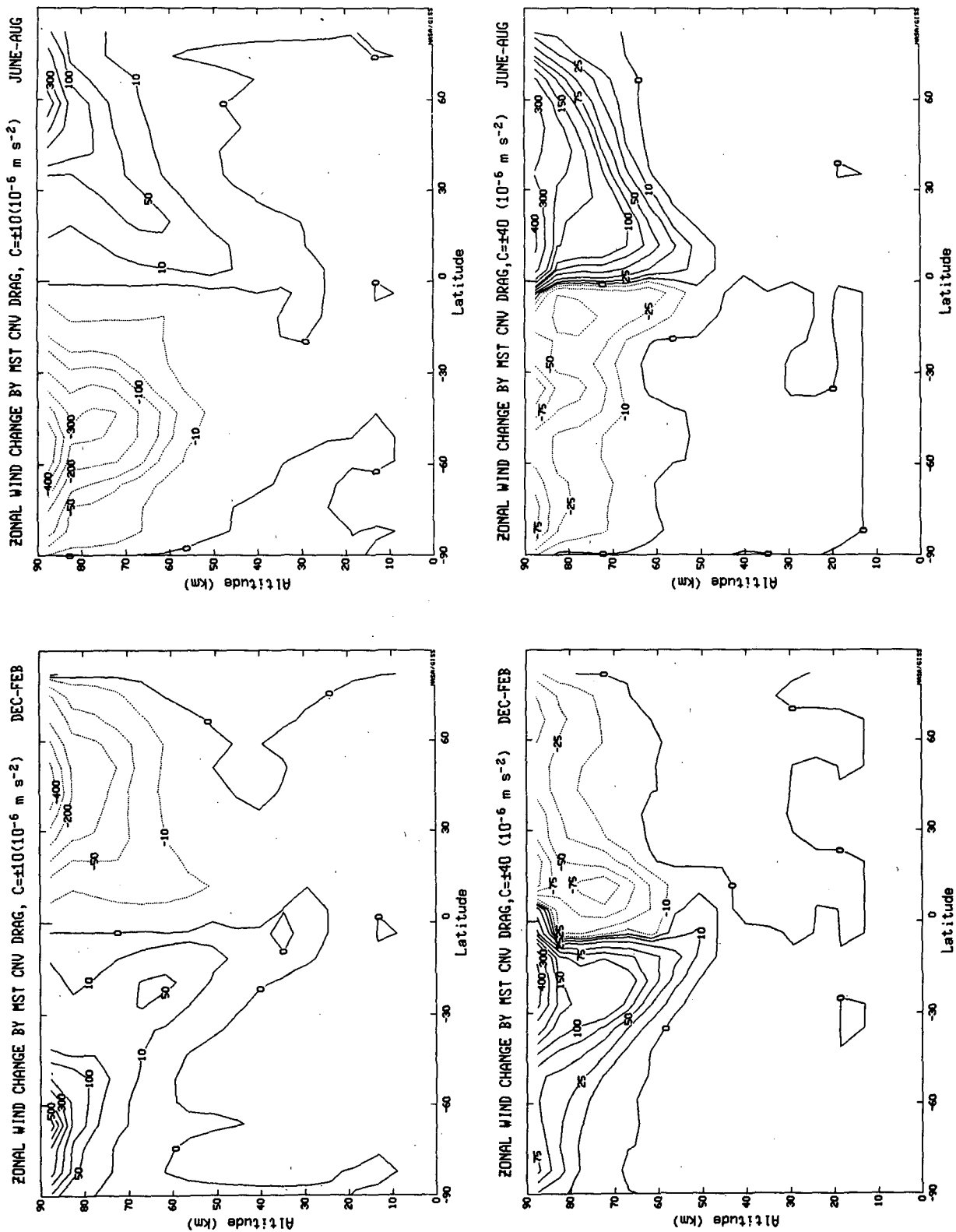


FIG. 6. As in Fig. 5 but for drag due to parameterized gravity waves from moist convection with phase speed = $V \pm 10 \text{ m s}^{-1}$ (top) and phase speed = $V \pm 40 \text{ m s}^{-1}$ (bottom).

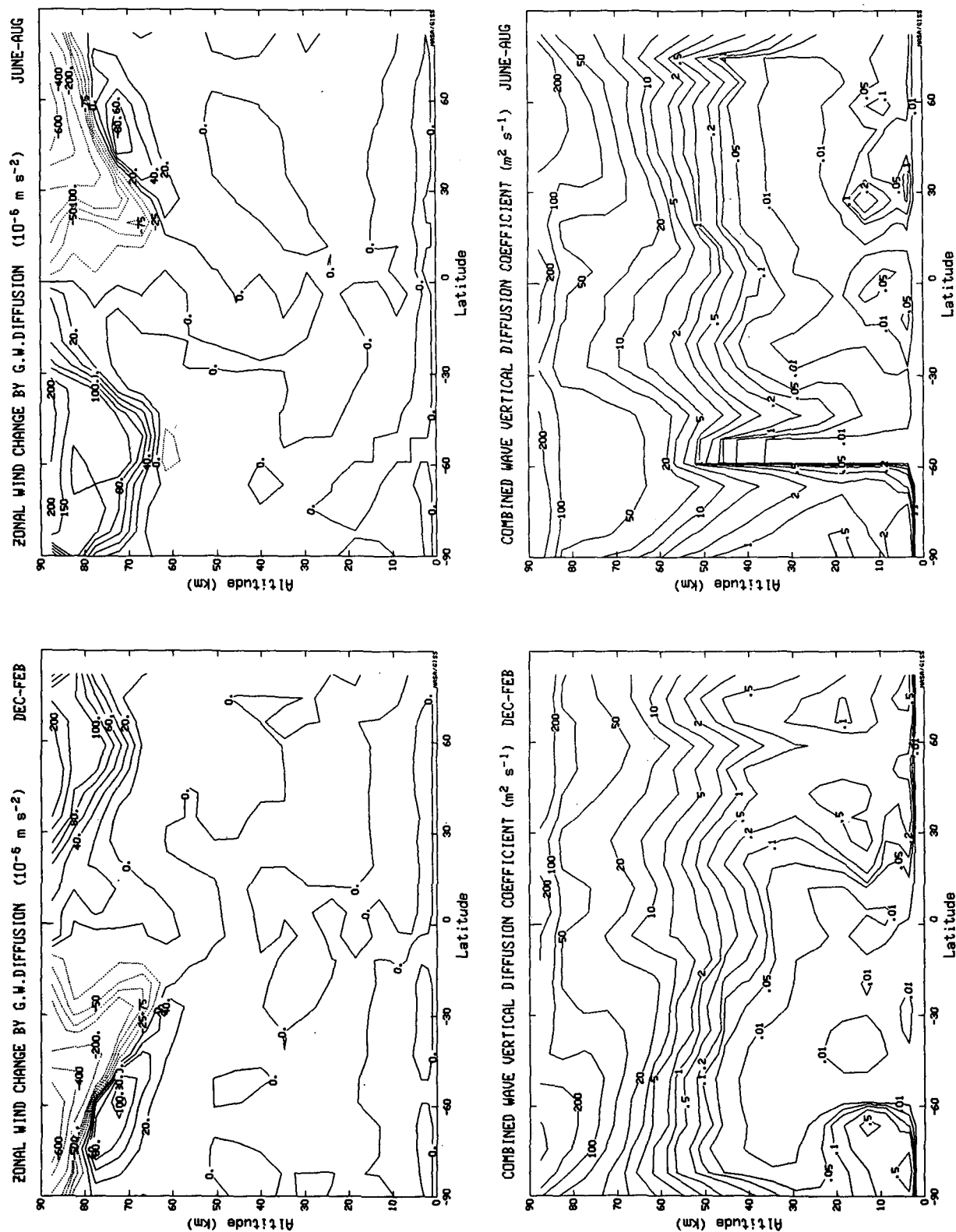


FIG. 7. Zonal wind change due to vertical diffusion associated with parameterized gravity wave breaking (top), and the combined wave vertical diffusion coefficients (bottom).

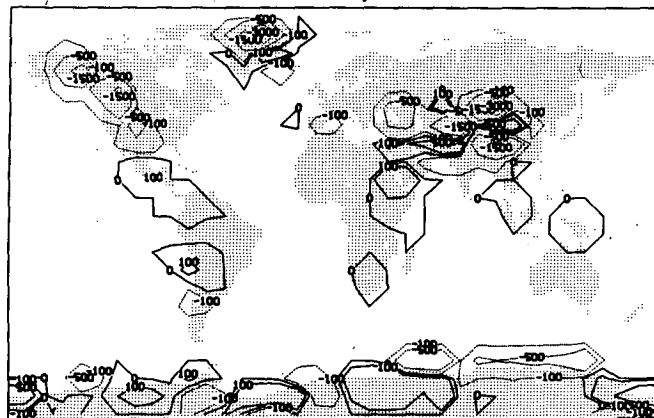
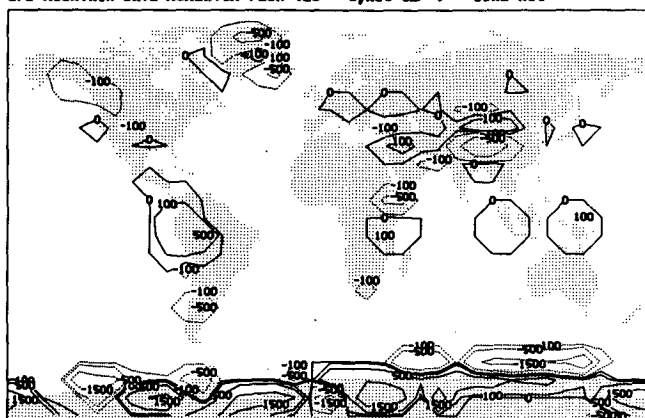
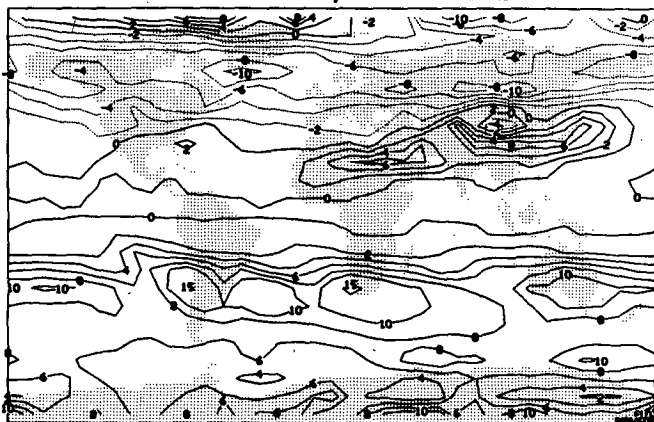
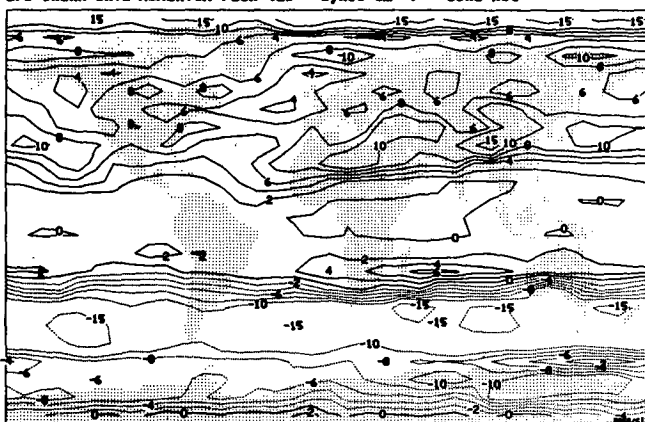
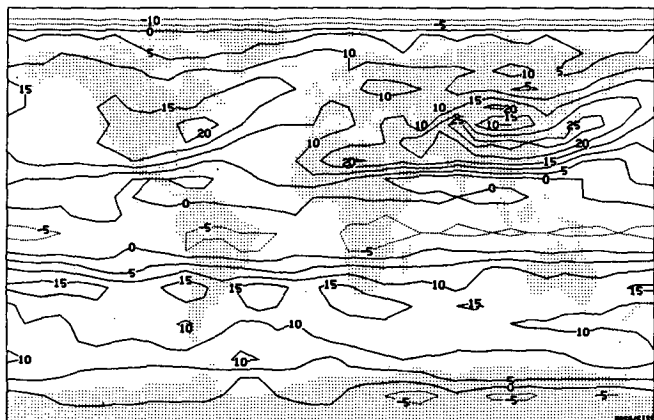
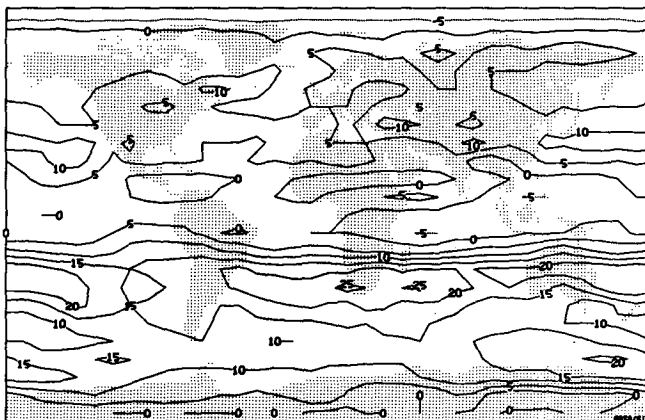
E/W MOUNTAIN WAVE MOMENTUM FLUX (10^{-3} dynes cm^{-2}) DEC-FEBE/W MOUNTAIN WAVE MOMENTUM FLUX (10^{-3} dynes cm^{-2}) JUNE-AUGE/W SHEAR WAVE MOMENTUM FLUX (10^{-3} dynes cm^{-2}) DEC-FEBE/W SHEAR WAVE MOMENTUM FLUX (10^{-3} dynes cm^{-2}) JUNE-AUGE/W COMPONENT OF SHEAR PHASE SPEED (m s^{-1}) DEC-FEBE/W COMPONENT OF SHEAR PHASE SPEED (m s^{-1}) JUNE-AUG

FIG. 8. Parameterized gravity wave zonal momentum flux from topography (top), and shear (middle), along with the shear wave phase speeds (bottom) for Dec-Feb (left) and Jun-Aug (right). Momentum fluxes are shown at the lowest level of application, 583 mb for the topographic waves, and 100 mb for the shear waves. The sign of the flux indicates its relationship relative to the winds at the application level, positive for eastward values.

vertical profile of the wind (Fig. 7; top). The vertical diffusion coefficients which result (Fig. 7, bottom) are in general agreement with those obtained from both dynamical (e.g., Ebel, 1984) and chemical (Allen et al., 1981) analyses, as well as the thermal and radio meteor

trail constraints (Johnson and Wilkins, 1965; Zimmerman, 1974). Also shown in Fig. 9 (bottom) are the momentum fluxes which propagate into the top layer of the model (close to the mesopause) and would affect the thermospheric circulation. These values represent

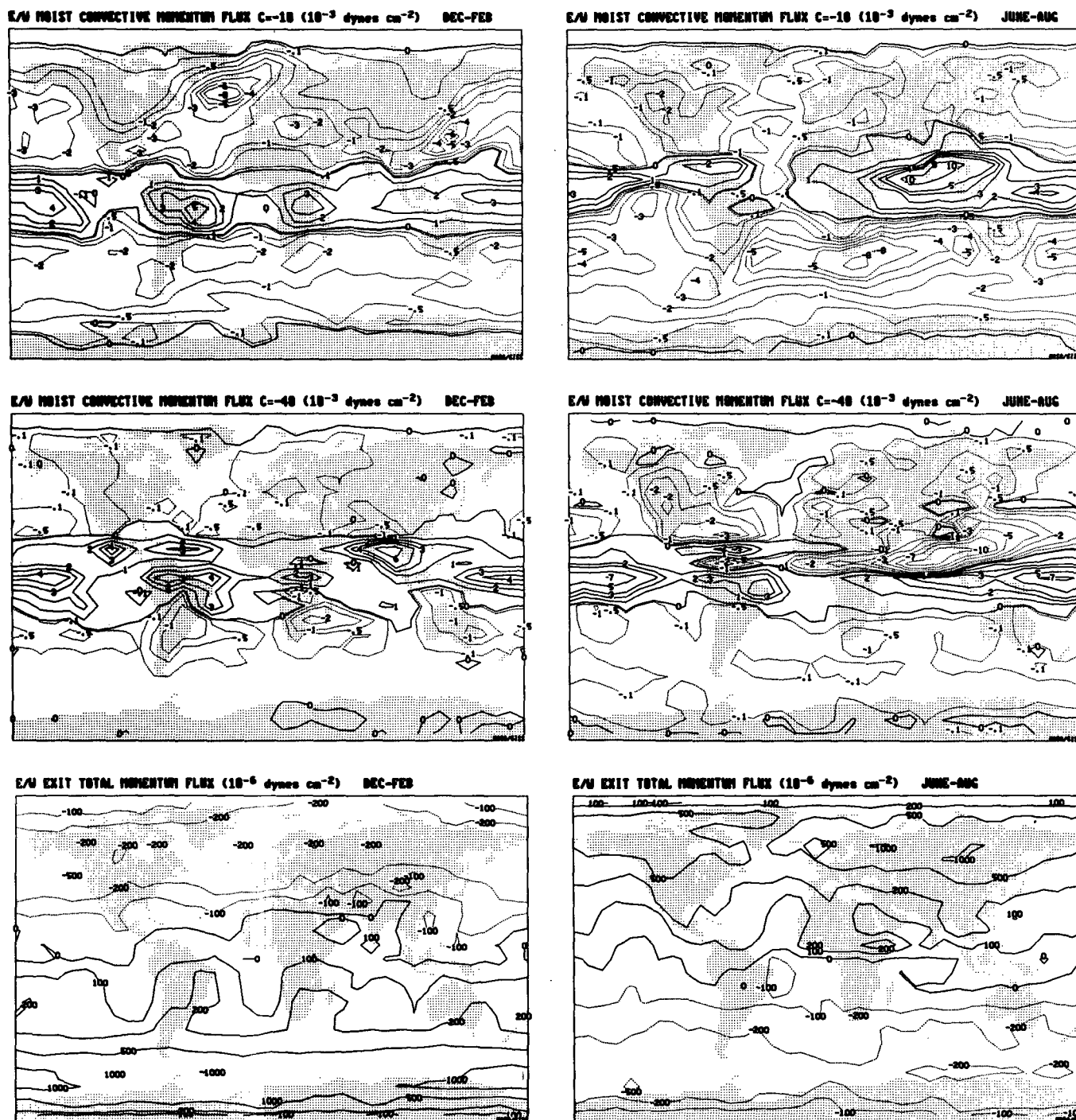


FIG. 9. Parameterized gravity wave zonal momentum flux at 100 mb from moist convection with phase velocity $c = V - 10 \text{ m s}^{-1}$ (top), from penetrating convection with $c = V - 40 \text{ m s}^{-1}$ (middle), and the zonal momentum flux that would reach the top layer of the model (bottom).

the model estimates of the gravity-wave fluxes appropriate for use in thermospheric models (e.g., Dickinson et al., 1984).

The gravity-wave parameterization includes radiative damping of the momentum flux, which produces

momentum convergence without diffusion throughout the middle atmosphere. The radiative damping contribution to the change of the wind is included in Figs. 5 and 6. It averages about 10% of the total gravity wave dissipation. Fels (1984) has emphasized that the radiative

tive damping effect consistent with his parameterization (which is used in this model) does not produce as great a damping as that employed in somewhat simpler models.

b. Temperature

The model-generated and observed temperatures as a function of latitude and altitude for the solstice seasons are shown in Fig. 10. The model successfully simulates the variation of the tropopause with latitude, including an accurate simulation of the lower stratospheric temperatures at upper midlatitudes of the winter hemisphere. The model temperatures agree with the observed temperatures throughout most of the stratosphere and mesosphere, including the cold summer and warm winter mesospheres. The model is not cold enough over the Southern Hemisphere winter pole between about 20 to 30 km, and is generally too cold in the two top levels (above 75 km). Potential reasons for these discrepancies are discussed below.

The seasonal distribution of model and observed temperatures in the lower stratosphere, upper stratosphere and mesosphere are presented in Fig. 11. Lower-stratosphere temperatures appear to be accurate except for the somewhat warmer values over the Southern Hemisphere winter pole (Fig. 11, top). (While the model values over the tropics also appear to be too warm, the observations shown are for a slightly lower level; interpolation of values to the 68 mb level of the model would have produced results in close agreement with model temperatures.) Temperatures in the upper stratosphere (Fig. 11, middle) also appear to be in good agreement, although values might be too cold over the Northern Hemisphere winter pole (this depends on the number and magnitude of stratospheric warmings which occur in the observed dataset). In the mesosphere the summer to winter temperature reversal is well simulated, but values in the tropics are somewhat too cold. This discrepancy is apparently due to the influence of the model top, and becomes more severe in the two highest layers (Fig. 10).

The change of the zonally averaged potential temperature with time in the middle atmosphere may be written as

$$\frac{\delta \bar{\theta}}{\delta t} = \frac{p_0^k}{p^k} (Q_{sw} - Q_{lw}) - \frac{\delta \bar{\theta}}{a \delta \phi} \bar{v}^* - \frac{\delta \bar{\theta}}{\delta p} \bar{\omega}^* - \frac{p_0^k}{p^k c_p} \frac{\delta V^2}{\delta t} + \frac{\delta(\bar{\omega}'\bar{\theta}')}{\delta p} \quad (26)$$

written as the sum of changes due to the shortwave heating rate and longwave cooling rate, transformed advection, kinetic energy dissipation associated with gravity-wave-induced drag, and the convergence of eddy sensible heat flux. The results for the different components are shown in Figs. 12–14. Solar radiation

heating rates indicate the slightly higher values during Dec–Feb due to the greater proximity of the earth to the sun during this season. The heating rates (Fig. 12, top) are in excellent agreement with those calculated by London (1980) but they are somewhat larger near the summer stratopause than those given by Gille and Lyjak (1986). As discussed by these authors, the difference appears to be the result of different ozone concentrations used in this area; this model uses the values of London (London et al., 1977) (see the discussion in section 2b). The thermal cooling rates agree well with those shown by Gille and Lyjak (1986) (the model temperatures are close to the LIMS values used in that study) as well as those calculated by Gartner and Memmesheimer (1984).

The temperature change due to the transformed advection is presented in Fig. 13 (top). The circulation produces rising motion and cooling in the summer mesosphere, and sinking motion with warming in the winter mesosphere. As noted above, the magnitude of this circulation is in general agreement with the available models and observations. Heating due to the dissipation of kinetic energy by the gravity-wave induced drag occurs throughout the mesosphere (Fig. 13, bottom); values are similar to those calculated by Gartner and Memmesheimer (1984) except near the summer polar mesopause, where the model indicates somewhat larger values. Despite the hemispheric asymmetry in heating by the transformed circulation, the total atmospheric dynamics, as produced in the model's "dynamics subroutine", produces cooling throughout the upper mesosphere (Fig. 14, top). The difference is the result of an additional cooling associated with the divergence of the eddy vertical sensible heat flux. Vertical sensible heat fluxes are downward throughout the mesosphere (Fig. 14, middle), as might be expected in a region of forced motion. However, the presence of a top to the model assures that no downward heat flux occurs at the top; this leads to a net divergence of heat in the upper mesosphere (Fig. 14, bottom), which acts to cool the model top layers, and produces values which are somewhat too cold above 75 km at all latitudes. It was to alleviate this difficulty that all the parameterized momentum flux which reaches the top layer is allowed to converge there, increasing the drag-induced warming at the model top by approximately 30%.

c. Eddy energy

Model and observed geopotential amplitudes of wavenumbers 1–3 in the Northern Hemisphere, and wave 1 in the Southern Hemisphere are shown in Figs. 15 and 16. While the model wave amplitudes are the proper order of magnitude, the values are somewhat too small (by about 30%) from the troposphere to the midstratosphere. This is a problem common to general circulation models (e.g., Mahlman and Umscheid, 1984), one which is not necessarily solved by going to

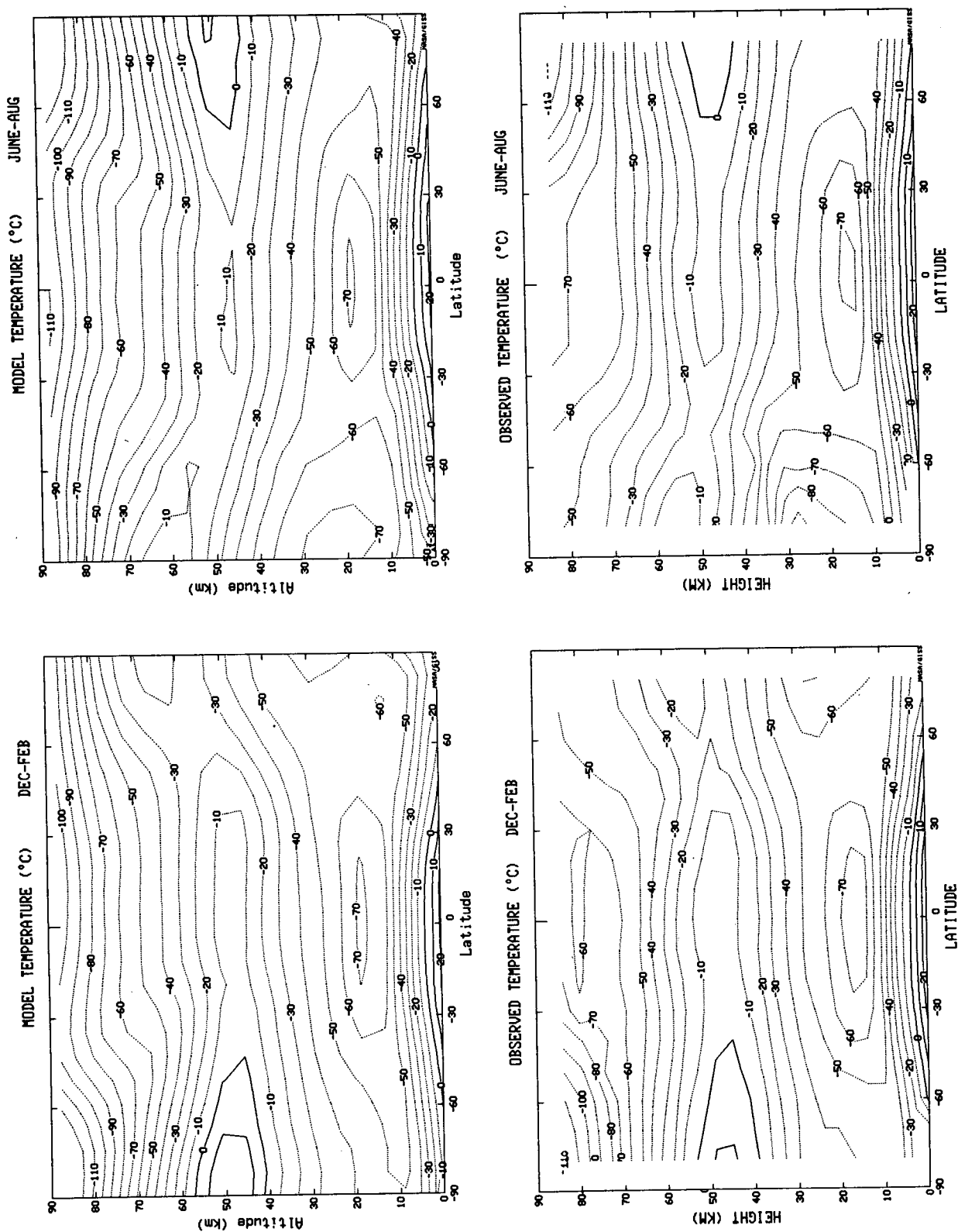


FIG. 10. As in Fig. 2 but for latitudinal average temperature versus height.

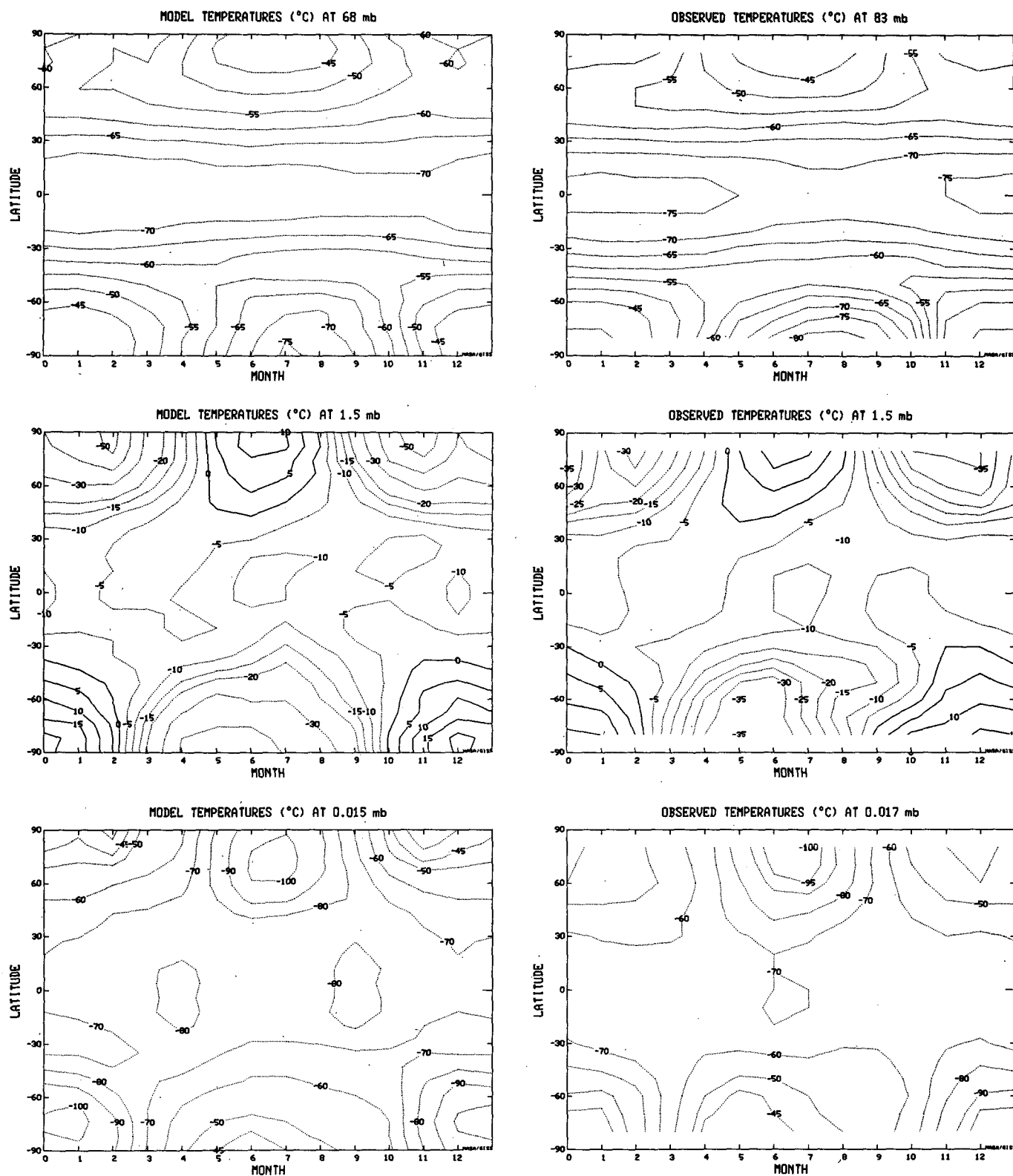


FIG. 11. As in Fig. 3 but for latitudinal average temperature versus month.

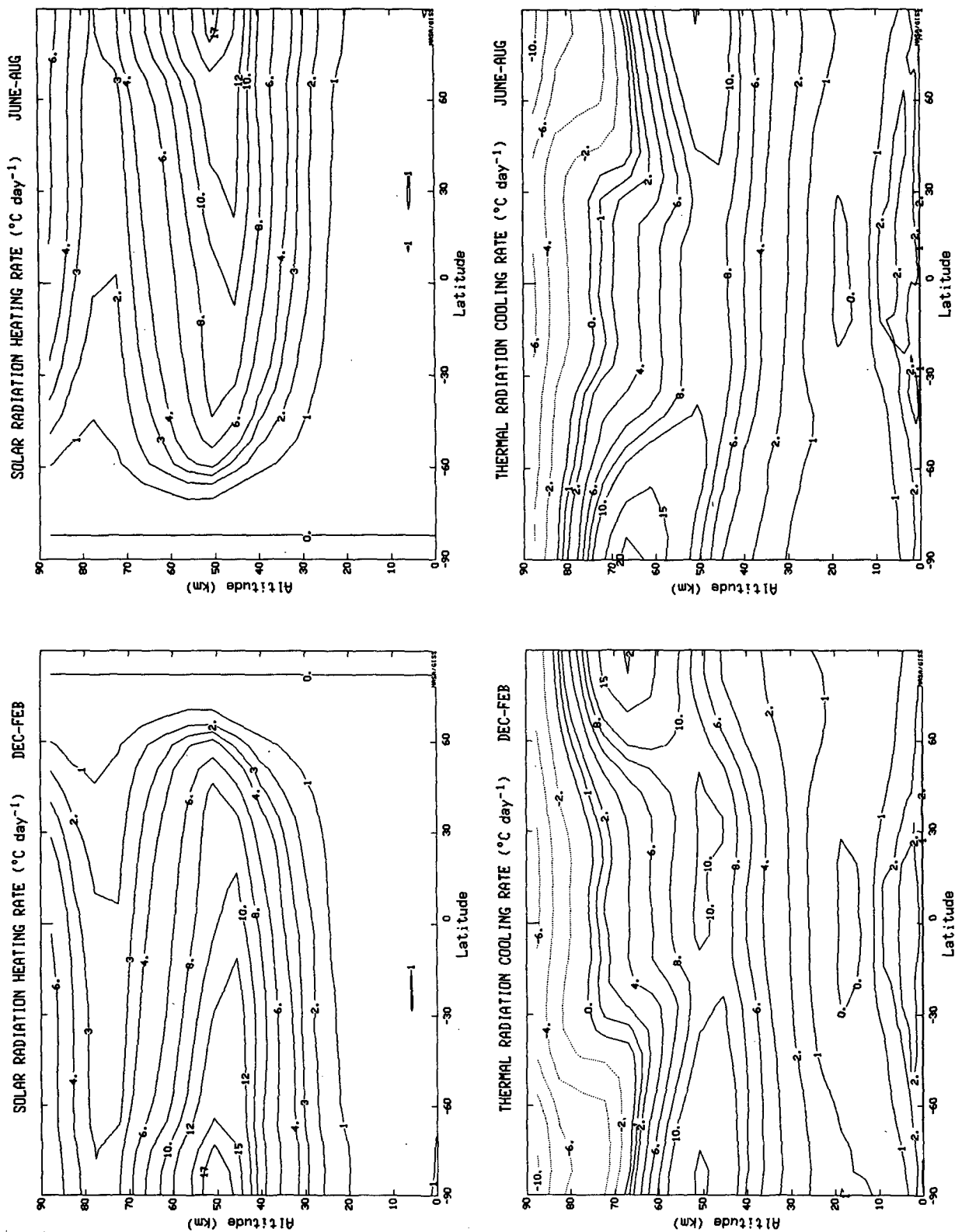


FIG. 12. Model solar radiation heating rates (top) and thermal radiation cooling rates (bottom) for Dec-Feb (left) and Jun-Aug (right). Negative numbers for cooling rates indicate heating.

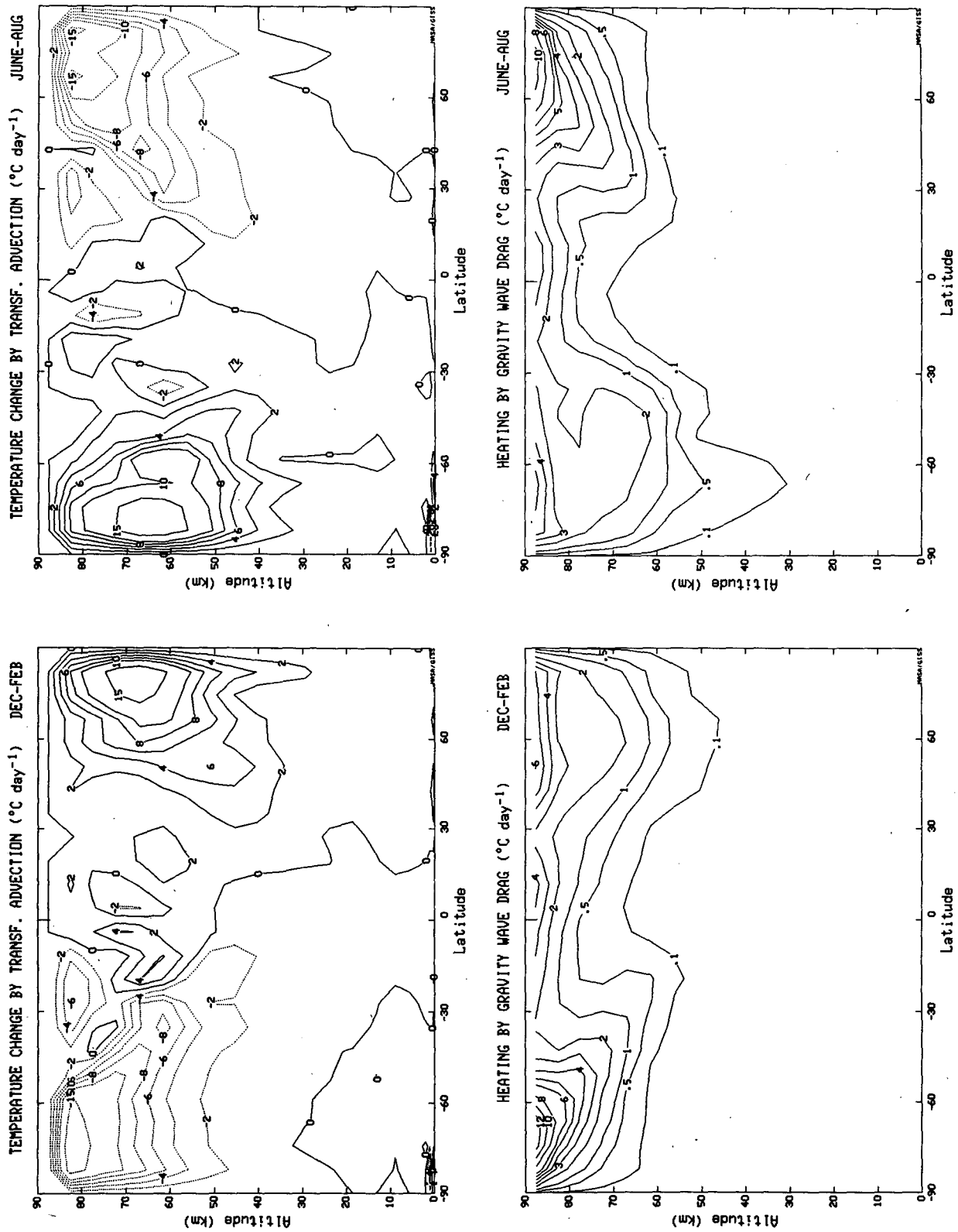


FIG. 13. Model temperature change by transformed advection (top) and heating by dissipation due to gravity wave drag (bottom) for Dec-Feb (left) and Jun-Aug (right).

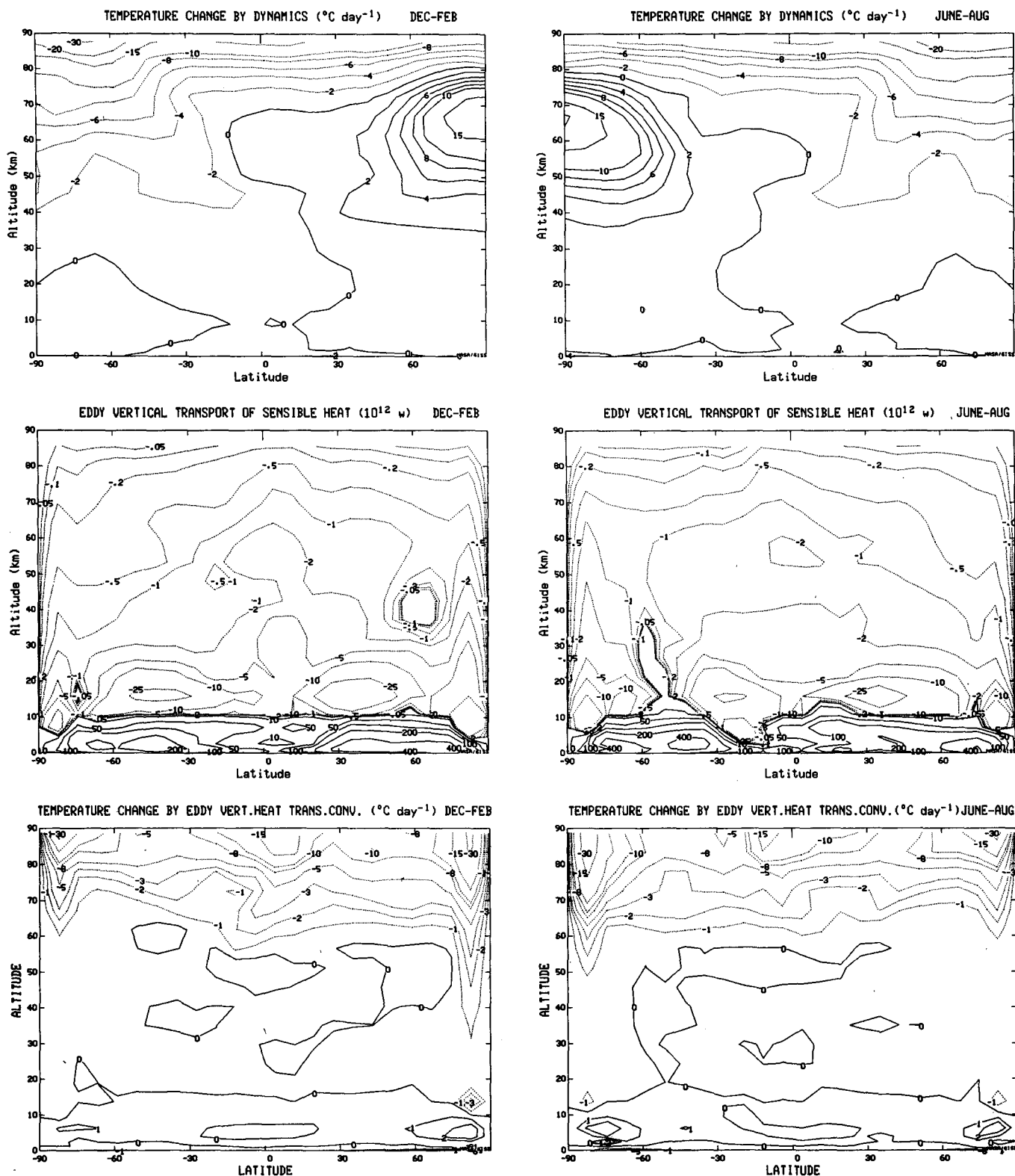


FIG. 14. Model temperature change occurring during the dynamics subroutine (top), eddy vertical transport of sensible heat (middle), and temperature change by eddy vertical heat flux divergence (bottom) for Dec-Feb (left) and Jun-Aug (right).

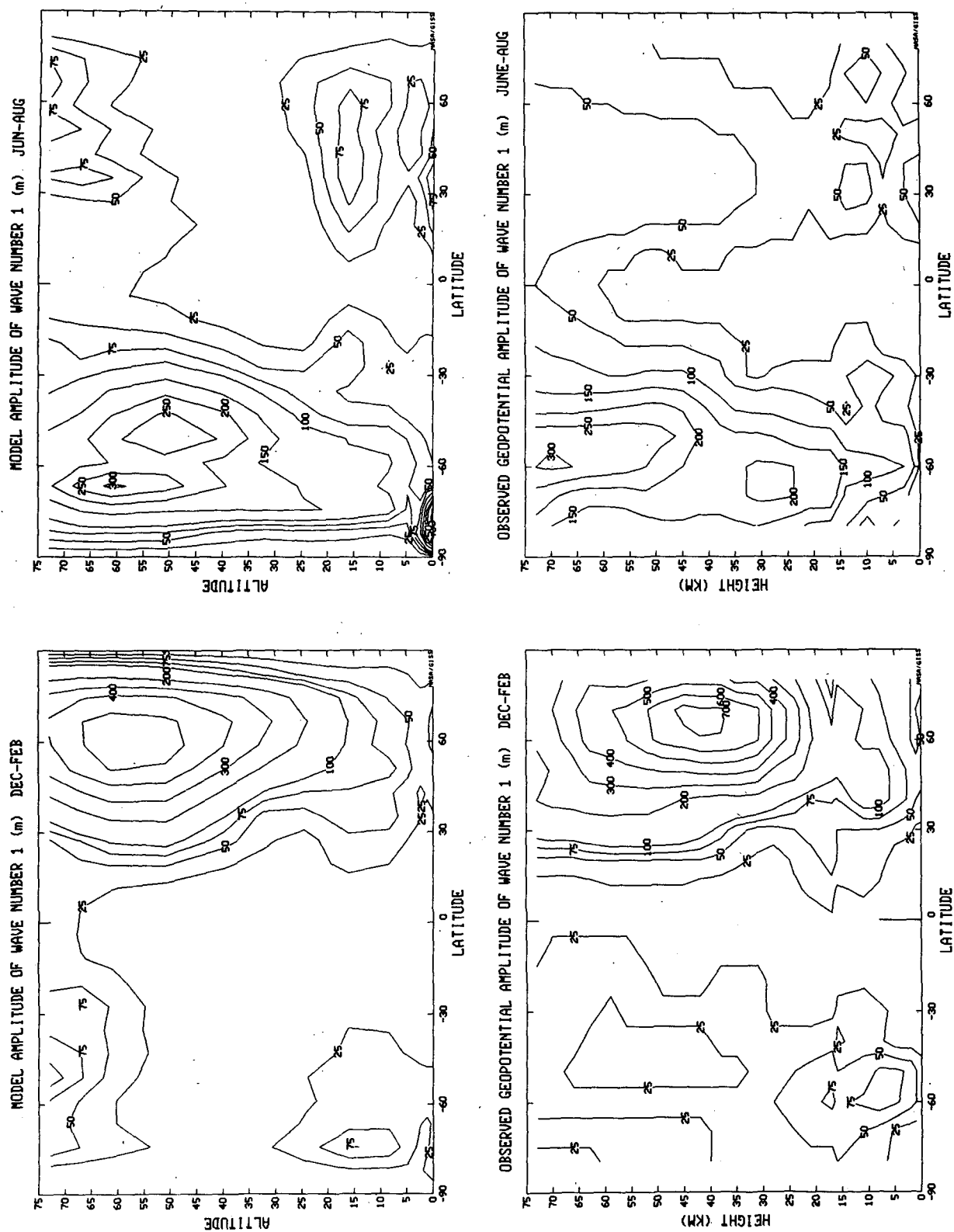


FIG. 15. Model (top) and observed (bottom) monthly average geopotential amplitudes of wavenumber 1 for Dec-Feb (left) and Jun-Aug (right). Observed values are from Smith (1983) and Barnett and Corney (1985b) for altitudes above 15 km, and from van Loon and Jenne (1972), van Loon et al. (1973), and Defant et al. (1979) for altitudes from 0–15 km. For the purpose of this comparison it is assumed the different observational datasets have consistent phasing.

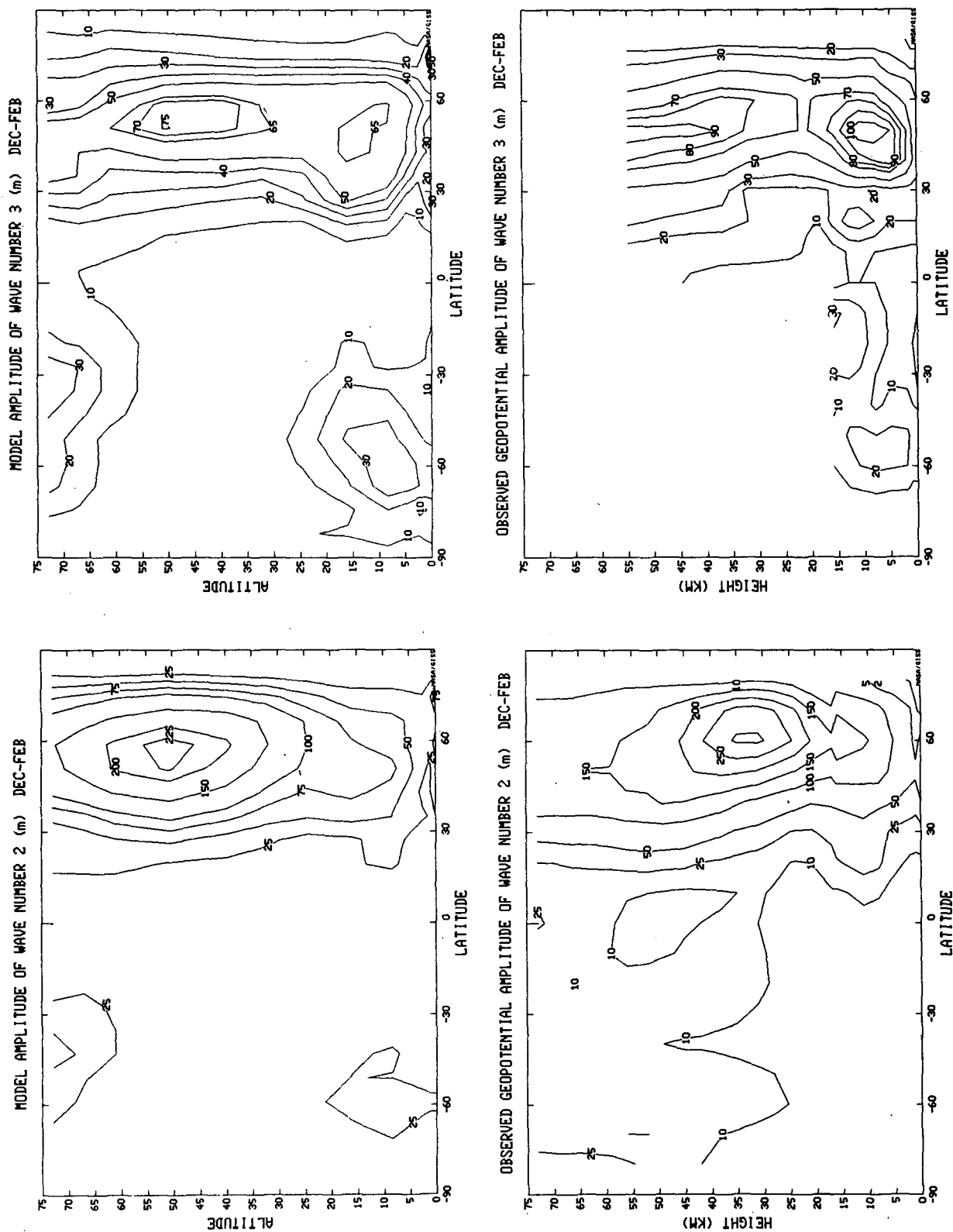


FIG. 16. Model (top) and observed (bottom) geopotential amplitudes of wavenumber 2 (left) and wavenumber 3 (right) for Dec-Feb. Observations from Barnett and Corney (1985b) above 15 km, and from sources listed for Fig. 15 below.

higher resolution. A comparison between observed and different GISS model values for the standing component of wavenumber 1 at 50°N during winter is given in Table 3. While the GCMAM values are within one standard deviation of the observed, they are uniformly low at pressures greater than 10 mb. Model 1 values were actually somewhat larger, although still deficient in the troposphere. The incorporation of gravity-wave drag has stabilized the lower stratosphere and reduced the eddy energy in the troposphere. In addition, it has also reduced the growth in wave amplitude with altitude. Both aspects combine to reduce the midstratosphere longwave energy in the model 2 version of the GCMAM. The nine-layer fine-grid model ($4^\circ \times 5^\circ$ resolution) has slightly more standing wave 1 energy in the troposphere than either the nine-layer medium-grid or the GCMAM.

The table also indicates that the long-wave energy in model 1 became excessive in the upper stratosphere, and that even in model 2 it grows relative to the observed with increasing altitude. As noted previously, the model may experience in situ wave generation in this region, and the EP flux divergences in the upper stratosphere were even larger in model 1. Alternatively, the model's dissipation or wave propagation characteristics may differ from those of the real world. It is not known how the use of zonally averaged ozone values in this model affects the longwave amplitudes.

As emphasized by Garcia and Geisler (1974), the wave amplitude is not a valid measure of the transmission of a wave through a level in which there is partial trapping. A more appropriate measure is the northward flux of sensible heat, which is related to the vertical flux of wave geopotential. Eddy northward transports of both sensible heat and momentum are compared with observations in Fig. 17. Again, while the results in general appear to be in good agreement, northward transports are somewhat too small in the low to midstratosphere, although the use of the geostrophic wind approximation in observations likely overestimates the observed eddy momentum transport (Robinson, 1986).

An alternate approach to looking at eddy energetics is to investigate the relevant terms in the energy cycle.

Model and observed winter energy values and conversions for the troposphere and lower stratosphere are shown in Table 4a, and model values for the upper stratosphere and mesosphere in Table 4b. Also shown are the interannual standard deviations (S.D.) of the model values. From Table 4a, it can be seen that the model's eddy kinetic energy (EKE) and vertical flux of eddy geopotential ($\omega'\theta'$) do not appear to be deficient in either the troposphere or lower stratosphere. As discussed by Rind (1986), the $8^\circ \times 10^\circ$ resolution probably produces too much energy in wavenumbers 5–9; energy in these wavenumbers would propagate vertically less effectively, and so produce less northward heat transport in the midstratosphere. The model energy spectrum for the lower stratosphere shows that about half of the model's total eddy energy, and one third of its standing energy, is in wavenumbers greater than wave 4.

Other features of interest indicated in Table 4a include reasonable model dissipation (D) values in the lower stratosphere, indicating that the mountain-wave dissipation is of the right order of magnitude; and reasonable interhemispheric differences in eddy kinetic energy (slightly more in the Northern Hemisphere) and zonal kinetic energy (ZKE) (more in the Southern Hemisphere lower stratosphere). The model lower stratosphere clearly represents the "refrigerator" effect referred to by Oort (1964) (although the model values are much larger), in which eddy kinetic energy is converted to eddy available potential energy ($C\{EAPE, EKE\}$ is negative). A similar energy cycle, with similar magnitudes of conversions and dissipation (within a factor of two) was reported by Kasahara and Sasamori (1974) using an earlier 12-layer version of the NCAR GCM.

In the upper stratosphere (Table 4b), the model atmosphere is distributing the upward flux of eddy geopotential energy into both eddy available potential and zonal kinetic energy, and in the mesosphere the upward flux goes primarily into eddy available potential energy and dissipation. However, as implied by the magnitude of the standard deviation relative to the mean value, in some months eddy kinetic energy in the upper stratosphere is being generated by dissipation, which

TABLE 3. Geopotential amplitude (m) of standing wave 1 at 50°N for Dec–Feb. SD: standard deviation, GCMAM: global climate middle atmosphere model; 9L: nine-layer model, M: medium grid ($8^\circ \times 10^\circ$ resolution), F: fine grid ($4^\circ \times 5^\circ$).

Pressure (mb)	Obs	Obs – SD	GCMAM	GCMAM – SD	Model 1	9L – M	9L – F
0.7	470	(225)	550	(220)	866		
3.4	480	(165)	400	(140)	615		
10	420	(146)	290	(94)	384		
30	230	(86)	180	(51)	197	147	187
100	120	(35)	93	(26)	107	77	83
300	120	(48)	62	(22)	93	103	108
500	90	(45)	49	(21)	66	74	79
700	70	(38)	42	(18)	37	44	58
850	60	(32)	45	(12)	26	30	54
1000	70	(26)	58	(18)	40	36	61

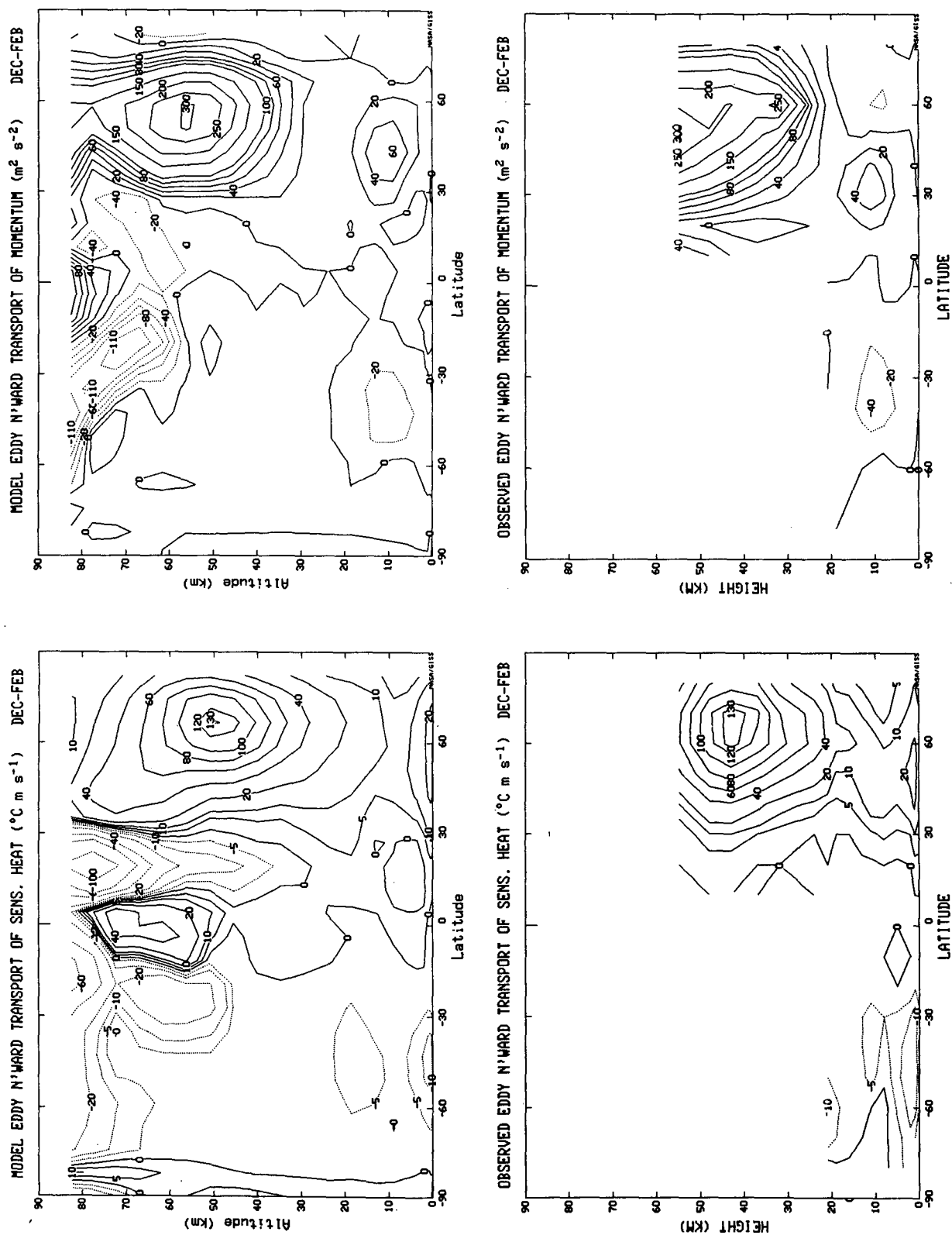


FIG. 17. Model (top) and observed (bottom) eddy northward transport of sensible heat (left) and momentum (right). Observed values are from Wu et al. (1984) for the Northern Hemisphere using the geostrophic wind approximation, and from Oort and Peixoto (1983a) for the Southern Hemisphere.

TABLE 4a. Model average monthly energy budget in northern winter. Z: zonal, E: eddy, KE: kinetic energy, APE: available potential energy, C: conversion, G: generation, D: dissipation of energy.

	Dec-Feb Northern Hemisphere			Jun-Aug Southern Hemisphere		
	Model	(SD)	Obs ^a	Model	(SD)	Obs ^a
Troposphere (984–100 mb) energy (10^6 J m^{-2}) C, G, D (W m^{-2})						
Stationary EKE	0.34	(.03)	0.20 ^e	0.31	(.05)	0.05 ^e
EKE	1.13	(.05)	0.88	1.08	(.05)	0.77
EAPE	2.75	(.06)	0.92	1.65	(.05)	0.55
ZKE	0.68	(.03)	0.80	1.07	(.04)	0.76
ZAPE	5.03	(.17)	5.64	8.38	(.34)	5.74
C{EAP, EKE}	2.85	(.22)	2.80	1.68	(.20)	2.10
C{EKE, ZKE}	0.09	(.13)	0.27	-0.42	(.11)	0.25
G{ZAPE}	5.81	(.34)		7.19	(.52)	
G{EAP}	2.24	(.27)		0.49	(.14)	
D{ZKE}	-0.68	(.05)	-0.48	-0.79	(.07)	-0.49
D{EKE}	-1.46	(.06)	-2.50	-1.39	(.11)	-1.90
	Model	(SD)	Obs ^{bc}	Model	(SD)	Obs ^d
Lower stratosphere (100–10 mb) energy (10^5 J m^{-2}) C, G, D (W m^{-2})						
Stationary EKE	0.31	(.04)	0.29 ^e	0.28	(.06)	0.05 ^e
EKE	1.13	(.07)	0.73	1.09	(.10)	0.67
EAPE	1.28	(.06)	0.47	0.78	(.03)	0.23
ZKE	0.80	(.14)	1.10	2.80	(.44)	4.20
ZAPE	0.78	(.09)	0.80	2.08	(.27)	1.80
C{EAP, EKE}	-3.10	(.25)	0.08	-1.70	(.20)	1.74
C{EKE, ZKE}	0.08	(.12)	0.09	0.30	(.30)	1.60
G{ZAPE}	-0.40	(.20)	-0.40	0.20	(.10)	2.31
G{EAP}	-0.60	(.20)	-0.60	-0.50	(.10)	-0.01
D{ZKE}	-0.67	(.10)	-0.76	-0.60	(.10)	
D{EKE}	-0.35	(.08)	-0.22	-0.20	(.10)	
$\omega' \phi'$ at 100 mb	4.25	(.40)	2.00	3.10	(.30)	1.70

^a Oort and Peixoto (1983a)^b Oort (1964) for winter, 1958^c Doplick (1971) for winter, 1964^d Hartmann (1977) for winter, 1973^e Estimated from Oort and Peixoto (1983b)

is consistent with the high-latitude EP flux divergence and negative potential vorticity gradients poleward of the jet (section 4a). Furthermore, in the mesosphere there is a tendency for in situ eddy energy conversion from the zonal kinetic energy, more prevalent on the hemispheric average in the Southern Hemisphere winter. Note the greater zonal kinetic energy in these regions during Southern Hemisphere winter, and the smaller amounts of eddy energy in the Southern Hemisphere at all levels, associated with reduced upward fluxes from the troposphere.

During Northern Hemisphere winter, the model has about 29% stationary eddy energy throughout the troposphere and stratosphere, dropping to 15% in the mesosphere. Observations show a slightly lower value in the troposphere, while in the stratosphere, Hirota (1976) using Nimbus 5 SCR radiance data for the 43 km level, estimated the standing wave component to be about 50% of the total for waves 1–3 at upper mid-

latitudes. Wu et al. (1984) compared sensible heat transports by stationary and transient eddies, and found stationary transports generally higher by a factor of 2–3 in the stratosphere. Model results show similar ratios in certain winter months, but give much smaller ratios in others. As indicated in Table 4b, the model standard deviation of stationary eddy energy ranges from 30%–40% of its mean value in the upper stratosphere and mesosphere, while for the total eddy energy the range is only from 7%–17%. It would be of interest to determine what the real atmospheric variability is, and whether the model's deficiency in standing wave energy and total eddy transports in the low and midstratosphere is associated with an occasional excess of transient eddy energy with inefficient transports.

In both model and observations, the phase of wave 1 shifts to the west with increasing altitude in the Northern Hemisphere during winter as the wave propagates vertically, but model phases appear to be some-

what west of the observed. This result can be seen by referring to the model geopotential heights at various pressure surfaces for the solstice seasons (Figs. 18, 19). The time-averaged Aleutian high is about 30° west of its observed position from 100–10 mb, although there is much variability in both model and observations. The deficiency starts in the troposphere; note that with this model resolution, the Aleutian low is too weak, and also too far west, although the Icelandic Low is well formed. The phase also shifts westward too rapidly with height in the stratosphere, consistent with the more rapid growth apparent in Table 3; differences between the model and actual wave propagation characteristics or in situ generation could be responsible. In contrast, Boville and Randel (1986) found that the phase of wave 1 shifted too slowly with height in the lower stratosphere in the NCAR community climate model (CCM). Symmetric circulations appear in both summer hemispheres, and the reduced standing wave energy during Southern Hemisphere winter is apparent.

d. Sensitivity experiments

In the course of development of the model, many sensitivity studies were performed to test model parameterizations. In this section we report on the changes produced in the model when the gravity-wave drag from the different sources is omitted. Additional results from sensitivity studies are noted in the discussion section. The gravity-wave drag is parameterized as occurring from three different tropospheric processes: flow over topography, shear, and convection. Also, the convective source is given additional phase velocities of $V \pm 20, \pm 40 \text{ m s}^{-1}$ for penetrating convection events. How necessary are these different sources, and how does the model change if they are omitted? To explore this issue, we have removed each of the sources, as well as the high-phase velocity convective source, independently, and run the model for three months starting in October of year 3. It is expected that the effects will be most pronounced during Northern Hemisphere winter, and it is our experience that this three-month period is sufficient to demonstrate a majority of the effects. Furthermore, December of year 3 experienced a stratospheric warming event, and we desired to see what effect elimination of the different drag mechanisms would have on this phenomenon. The results of the different experiments for the third month are shown in Figs. 20 and 21; the effects on the stratospheric warming will be discussed in more detail in Part II (Rind et al., 1988).

Without mountain drag, west winds increase throughout the winter stratosphere (Fig. 20, left top). In the lower stratosphere there is now no clear separation between the tropospheric and stratospheric jets. Consistent with the continual positive west wind shear with height, high-latitude temperatures in the lower stratosphere are $5\text{--}15^\circ\text{C}$ colder, and the high-latitude

TABLE 4b. Model average monthly energy budget in winter.

	Dec-Feb Northern Hemisphere		Jun-Aug Southern Hemisphere C, D, G	
	Model	(SD)	Model	(SD)
Upper Stratosphere (10–0.46 mb) energy (10^4 J m^{-2}) (10^{-2} W m^{-2})				
Stationary EKE	0.79	(0.24)	0.56	(0.36)
EKE	2.75	(0.47)	2.50	(0.57)
EAPE	1.53	(0.16)	0.81	(0.07)
ZKE	2.98	(0.71)	8.30	(2.10)
ZAPE	1.69	(0.47)	2.90	(0.49)
C{EAP, EKE}	–2.60	(1.40)	–4.00	(1.00)
C{EKE, ZKE}	3.10	(1.20)	3.00	(1.00)
G{ZAPE}	3.60	(0.30)	4.00	(0.10)
G{EAP}	–2.00	(0.60)	–1.00	(0.30)
D{ZKE}	–1.14	(0.50)	–4.00	(1.00)
D{EKE}	–0.20	(0.80)	–0.10	(0.30)
$\omega'\phi'$ at 10 mb	7.80	(2.00)	7.00	(2.00)
Mesosphere (0.46–0.001 mb) energy (10^3 J m^{-2}) C, D, G (10^{-2} W m^{-2})				
Stationary EKE	0.71	(0.28)	0.42	(0.14)
EKE	4.83	(0.35)	3.80	(0.19)
EAP	0.51	(0.04)	0.24	(0.03)
ZKE	4.79	(1.37)	5.80	(0.86)
ZAP	0.16	(0.04)	0.20	(0.04)
C{EAP, EKE}	–1.40	(0.30)	–2.00	(0.20)
C{EKE, ZKE}	0.15	(0.20)	–0.60	(0.20)
G{ZAP}	0.63	(3.10)	–0.15	(0.10)
G{EAP}	–0.16	(5.20)	–0.10	(0.01)
D{ZKE}	–1.30	(0.50)	–3.00	(0.60)
D{EKE}	–0.60	(0.15)	–0.40	(0.10)
$\omega'\phi'$ at 0.46 mb	2.60	(0.50)	2.00	(0.30)

tropopause is at too high an altitude. It is clear that the inclusion of mountain drag is responsible for the improvements in the simulations of the lower stratosphere in model 2 compared to model 1. The drag imparted by the topography in the lower stratosphere is especially important in the GISS model, which does not include any other explicit momentum dissipation in this region (i.e., no numerical diffusion). Although the mountain drag does not play a dominant role in the model in controlling the winds at upper levels, its elimination did allow the winter westerlies and high-latitude summer easterlies to increase somewhat near the model top; the contribution of the other drag mechanisms responded in an opposite sense, especially the shear drag which increased dramatically in the summer hemisphere (Fig. 20, bottom). The wind deceleration is proportional to $(U - c)^3$ (Eq. 16), so when one drag process is removed and the wind increases, the deceleration from other processes becomes larger as long as those remaining waves can still break. The proportionally greater response of the other drag mechanisms also illustrates that the effectiveness of the drag cannot

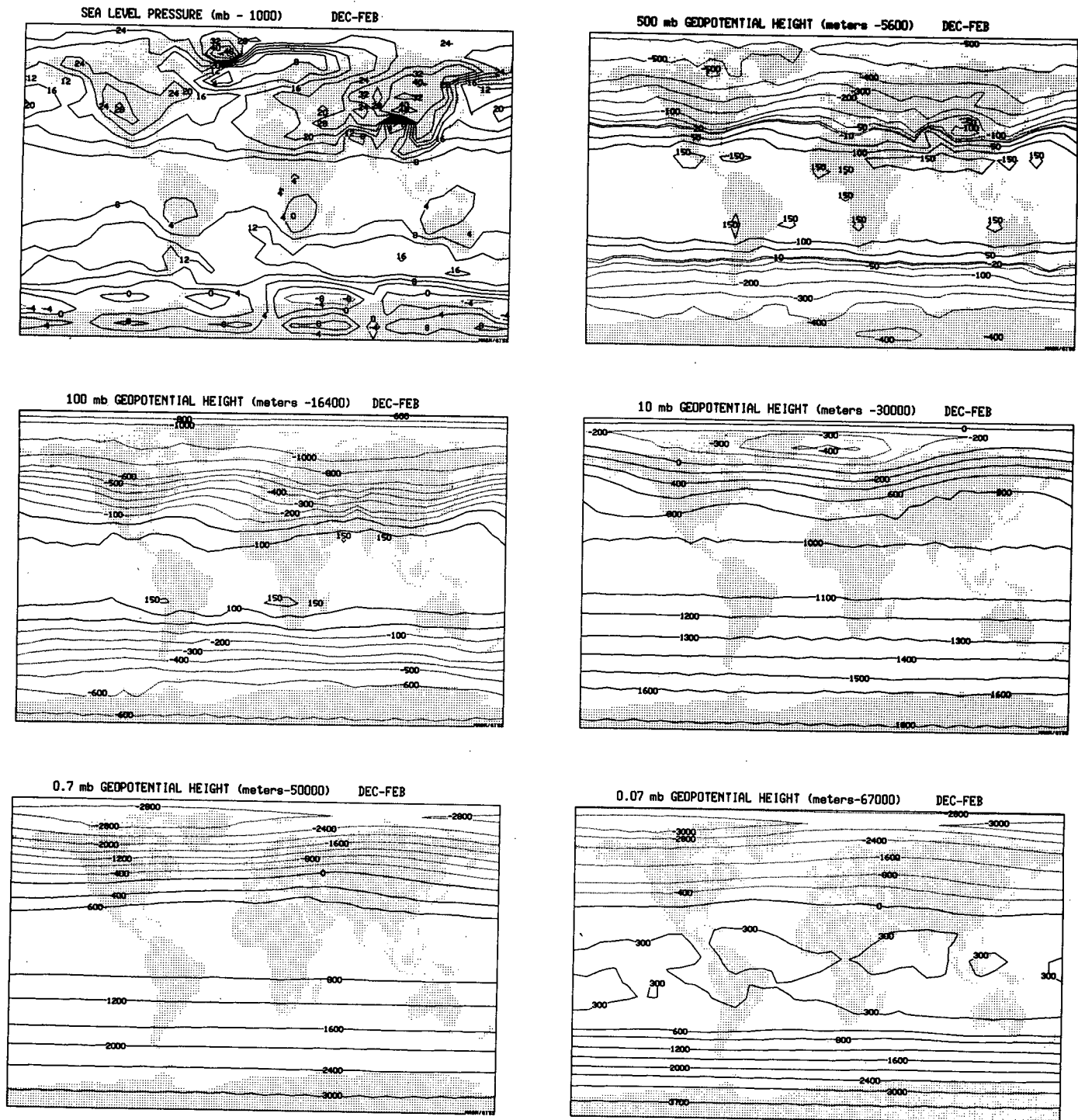


FIG. 18. Model Dec-Feb sea level pressure (top left), and geopotential height fields at 500 mb (top right), 100 mb (middle left), 10 mb (middle right), 0.7 mb (bottom left), and 0.07 mb (bottom right).

simply be measured by the change of wind it induces; the zero phase velocity associated with the mountain waves effectively keeps the wind from accelerating, and so minimizes the necessity for large wind changes due to wave breaking [Eq. (4)].

As noted in the introduction, several groups (UKMO, CCC) are using gravity-wave parameterizations associated with topography to improve the tropospheric circulation, specifically the tendency for high-resolution models to develop excessively deep low-

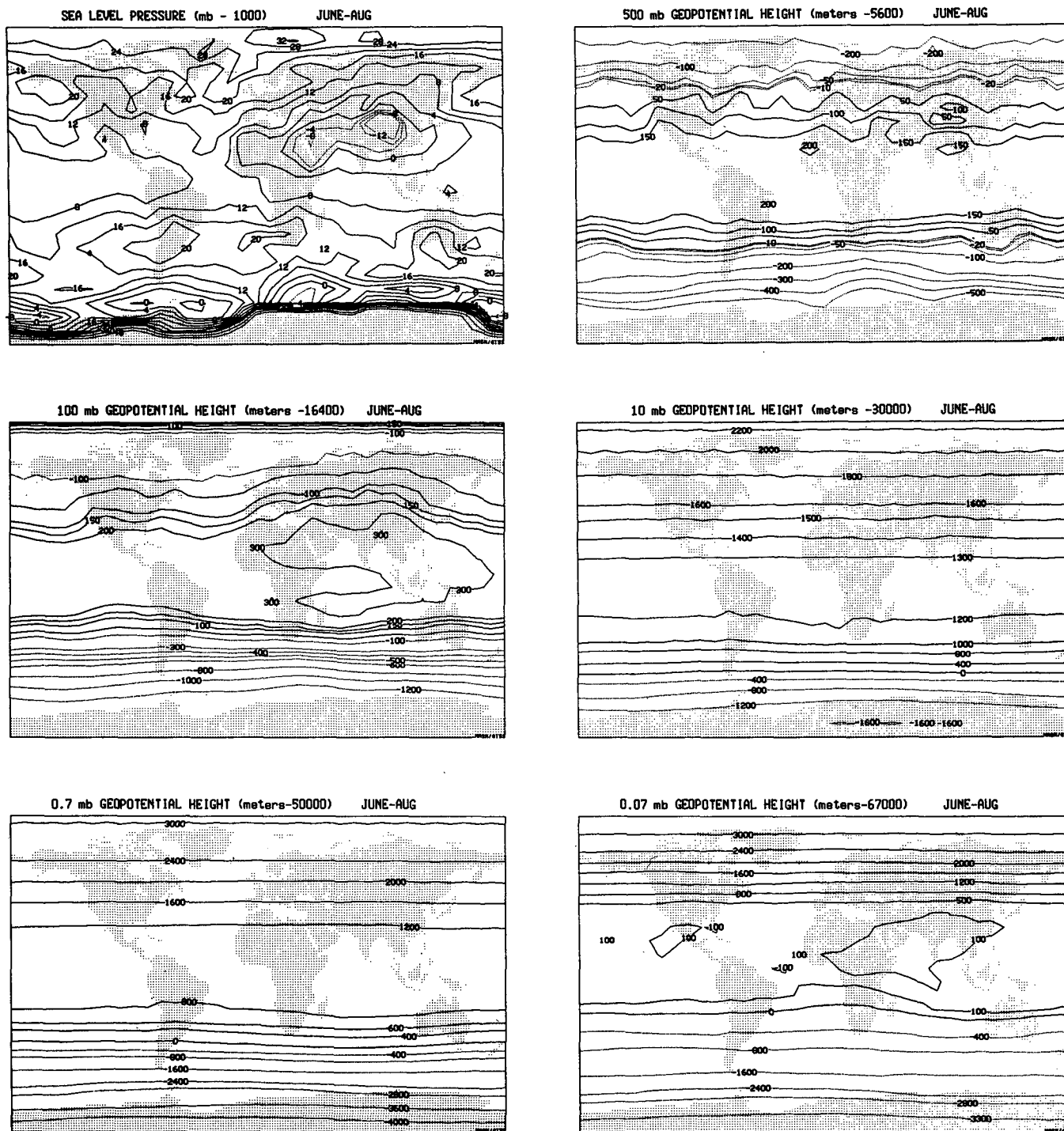


FIG. 19. As in Fig. 19 but for Jun-Aug.

pressure areas over the North Atlantic and Pacific oceans. The depth of these lows has been shown to be inversely related to the stability in the upper troposphere (Hansen et al., 1983); as the gravity-wave damping increases the stability, the subpolar lows decrease in intensity. Without mountain wave drag, the

GCMAM also produced deeper subpolar lows, but the coarse-resolution model tends to underestimate the strength of these lows normally (e.g., Fig. 18). In the experiment without mountain drag, the subpolar lows were slightly better defined, and thus more realistic.

The removal of shear drag has a large impact on the

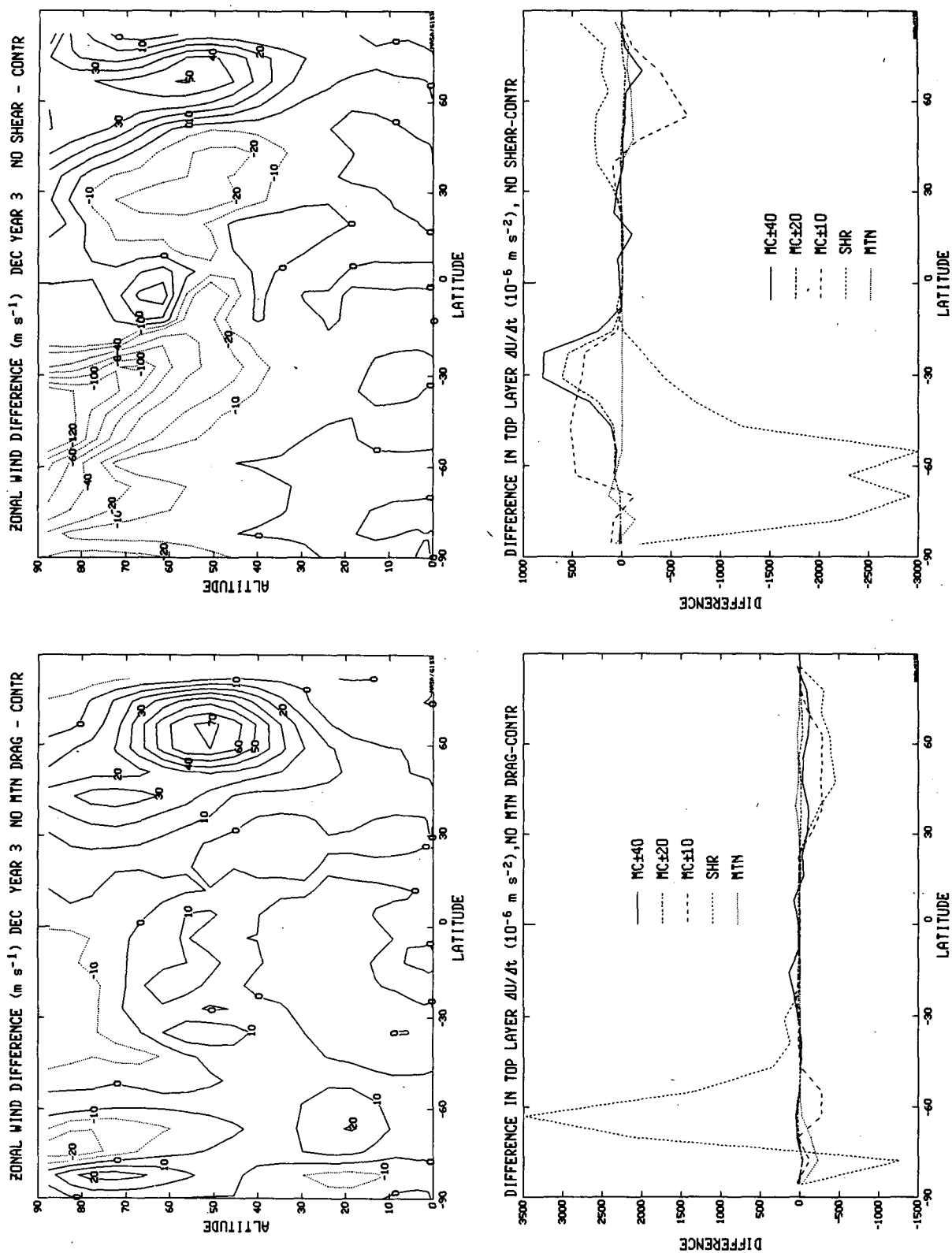


FIG. 20. Change in the zonal wind (top) and in the drag by different parameterized gravity wave components in the top layer (bottom) during the third month (December) of the experiment with no parameterized gravity waves due to topography (left) or due to shear (right).

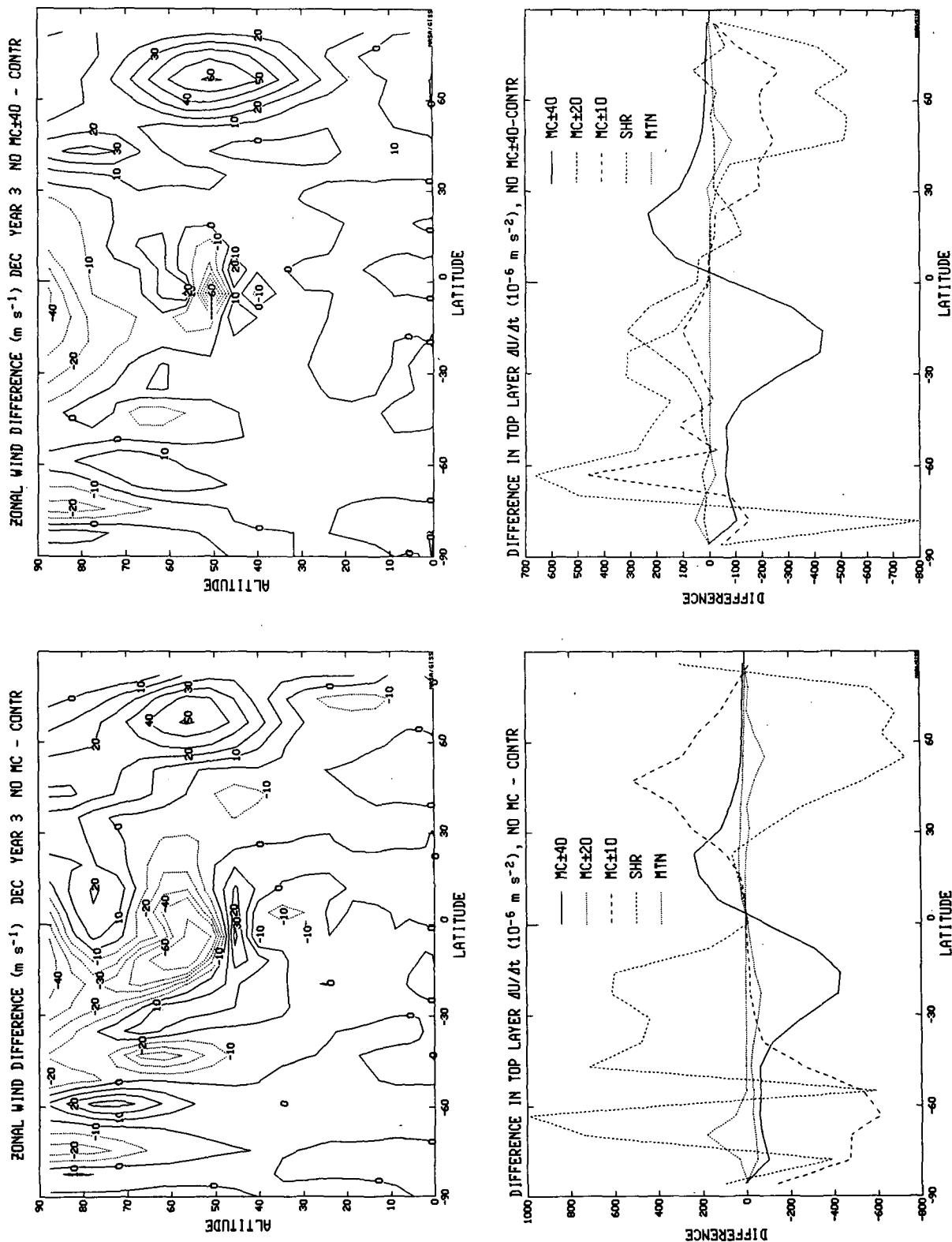


FIG. 21. As in Fig. 20 but for no parameterized gravity waves due to convection (left) or due to convection with $c = V \pm 40 \text{ m s}^{-1}$ (right).

mesospheric circulations in both hemispheres (Fig. 20, top right). In the winter hemisphere westerlies increase, and values for November reach 125 m s^{-1} ; in the summer hemisphere easterlies accelerate to very large values near the model top. The difference in drag in the top layer due to this experiment (Fig. 20, right bottom) clearly shows that the lack of shear drag deceleration in the summer hemisphere cannot be made up for by the other drag mechanisms, and the summer pole to winter pole circulation is accelerated by the Coriolis force to produce very large east winds.

The removal of moist convective drag has a major impact on the tropical circulation of the lower mesosphere (Fig. 21, top left). The moist convective waves are decelerating the tropical easterlies, and thus are partly responsible for the improvement in the lower-mesosphere zonal wind structure in comparison with model 1 (Fig. 1). This experiment has less of an obvious oscillation in the tropical wind field, although the apparent smoothing may be simply the result of the dominance of the generated easterlies. Comparison of this experiment with an experiment which removed only the high-phase velocity moist convective waves (Fig. 21, top right) shows that these latter waves are responsible for decelerating the equatorial east winds near the model top, as well as a geographically more restrictive region of easterlies in the lower mesosphere. While moist convective waves do influence the upper-level winds at other latitudes, the shear waves appear capable of making up the deficit outside of the tropics.

All of the experiments produce substantially greater west winds in the winter stratospheric jet region in December. This difference results from the impact of the different drag mechanisms on the stratospheric warming during the month, and will be discussed in more detail in Part II (Rind et al., 1988).

5. Discussion

The results show that the GCMAM as currently constituted produces a reasonable simulation of the stratosphere. Improvements over the previous version of the model have been achieved largely through the incorporation of the parameterized gravity wave drag. The deficiencies that have been isolated are somewhat reduced long-wave energy in the lower stratosphere, with wave 1 phase about 30° west of the observed; possibly excessive oscillations in the equatorial wind field near the stratopause; too cold temperatures near the top of the model; and too warm temperatures in the Southern Hemisphere polar stratosphere. In this section we will discuss a variety of questions related to the gravity wave parameterization, as well as other aspects of stratospheric modeling, including a discussion of the possible reasons and remedies for the deficiencies. This section is based on a number of sensitivity studies conducted in the course of the model development.

a. Gravity wave parameterization

While the gravity wave parameterization improved the model significantly, there are many difficulties and choices involved in its implementation. As implied by the expression for the saturation momentum flux (Eq. 10), the relationship between wave breaking and the background wind exhibits strong positive feedback. If the wind velocity is large, the momentum flux required for saturation is similarly large, and there is less possibility that the parameterized waves will break. If the waves do not break, there is little momentum deposition. [Only the gravity-wave radiative damping occurs, and even this tends to be small since the vertical group velocity, Eq. (11), also becomes large.] With little effective drag, the background winds become even larger. In effect, once the winds accelerate sufficiently, they then remain excessive for the rest of the season. Not only does this leave little room for error, it also implies that simulations of at least several months are necessary for each experiment. In practice, we have found it necessary to start each run on 1 September, before winds in the stratosphere have begun to accelerate, so that the parameterized waves will have a chance to break. It is then necessary to continue the simulation through December, or preferably January, to obtain a true indication of how the winter winds will ultimately react. If this procedure is not followed, it is possible, and even likely, that upon integrating through the annual cycle, the subsequent winter will bear little resemblance to the preceding one, in terms of the effect of the parameterization.

This "all or nothing" aspect is further exaggerated by the choice of relatively short wavelengths (on the order of 200 km). Lindzen (1984) estimated horizontal wavelengths for gravity waves of 1000 km, but observations often point to smaller values (e.g., Vincent and Reid, 1983). As indicated in Eq. (16), the deceleration of the background wind is directly proportional to the wavenumber; shorter waves produce a much stronger impact, and are thus more "difficult to handle". Decelerations were sufficiently large in the mesosphere that it was deemed necessary to include the parameterized drag in the dynamics, using a forward time step in parallel with the leapfrog time steps of the pressure-gradient force and advection terms. That allowed the pressure gradient and other terms to react on a short time scale, and produced more stable calculations. An additional problem which arises in this regard is that a somewhat different formulation proved necessary to include the vertical diffusion in the dynamics; we use a simplified implicit scheme for added stability. Note that to conserve angular momentum, the parameterized gravity-wave momentum flux should be subtracted from the surface drag; in latitudes of large topography, the peak gravity-wave momentum flux ranges from 10–30% of the surface drag effect, a nonnegligible cor-

rection. However, the surface drag is calculated in its own self-consistent routine, and no correction was applied in this model.

The mountain-wave parameterization severely restricted the range of topography variance which was allowed. If too small topography is permitted to generate mountain waves, the winter stratospheric jet and longwave amplitudes are reduced to small values. This is at least partially the result of our assumption of monochromatic waves; as emphasized by Schoeberl (1985a), the variation in the vertical group velocity with wavelength will cause the effective gravity-wave amplitude(s) to diminish with height, and raise their breaking level. Such an effect, however, would then provide cumulatively excessive breaking at the higher levels if all regions of topography variance were allowed to generate mountain waves.

If too large values of topography are included, the drag becomes excessive in the lower stratosphere, which has the effect of overstabilizing the troposphere. This parameterization can alter the tropospheric eddy kinetic energy by 33% due entirely to its effect in the lower stratosphere. As noted in Hansen et al. (1983), in the nine-layer model the strength of the Aleutian Low was directly proportional to the upper-tropospheric stability and the strength of the drag. The current version of the GCMAM has about 25% less eddy energy in the troposphere than did model 1 with its excessively small upper-tropospheric stability, an effect which can be seen to some extent in Table 3. McFarlane (personal communication) has suggested that momentum fluxes might in practice be limited by restricting the topography variance to scales smaller than about 200 km due to the reducing effect of rotation on surface momentum fluxes, and by restricting the variance locally to be no larger than that which would give a local Froude number ($Fr = Nh/U$) of order unity, because of upstream blocking effects. These possibilities may account for our practical need to place an upper limit on the allowed topography variance.

One additional impact that strong mountain drag has on the model is to tend to induce a rapid phase shift with height of the long waves. Consider a background wave and its associated longitudinal wind distribution, with widely separated regions of weak and strong winds. The parameterized gravity wave will be more likely to break in the region of weak winds; once having broken, it will be less likely to break in the levels immediately above, so winds at these higher levels will increase. The opposite effect will hold true in the vicinity of the strong winds where the waves do not break; immediately above the strong wind region there will be a greater tendency for breaking and slowing of the winds. The rapid variation in the vertical of the longitude of maximum and minimum wind location is in effect a rapid phase shift with height of the wave. It does not appear as if the excessive phase shift with

height of wave 1 in model 2 is the result of this process as the same problem occurred in model 1 (without gravity-wave drag), at least in the low and midstratosphere.

Model temperatures are too warm in the Southern Hemisphere polar stratosphere (Fig. 10). This was not true in model 1, although that may be a case of getting the right answer for the wrong reason: temperatures throughout high latitudes were too cold in that model. The warm temperatures seem to be associated with the mountain drag which occurs above Antarctica (Fig. 5), and it raises the question of whether the mountain-drag parameterization is accurate over regions of such consistently high topography. One additional effect which is missing in the model and which may influence this problem has to do with cloud generation. The model is not allowed to form clouds in the lower stratosphere (although condensation may occur), and polar stratospheric clouds are known to exist in this region at very cold temperatures (McCormick et al., 1982). The clouds in fact will produce additional cooling, and it may be that the clouds are having a significant impact on the temperature at which they are observed. The feedback is probably positive; at cold temperatures the moisture supersaturates, a cloud develops, the region then cools further, greater supersaturation exists, etc. Were this effect possible in the model, temperatures might be lower.

As indicated by the sensitivity experiments, the shear-induced gravity wave parameterization is of utmost importance for the summer hemisphere mesosphere. The strength of the mesospheric summer easterlies, especially at high altitudes and latitudes, is directly related to the latitudinal distribution of the shear wave breaking. If the latitudinal gradient, with increased shear drag at lower latitudes, is too strong, the drag itself sets up local meridional circulations. The equatorward-moving air is accelerated by the Coriolis force and produces extremely high values of east winds. We believe that one of the reasons for the excessively large easterlies in the tropical lower mesosphere of model 1 was that the modified Rayleigh friction used in that model, with drag everywhere and directly proportional to the background wind speed, tended to produce large gradients of the drag. The sensitivity of the shear drag is particularly evident in the results of the no mountain-drag experiment, where despite an apparently small change in drag by other mechanisms, the summer shear drag showed a large variation. Note we are only using one shear-generated wave at each location, that wave which will propagate into the mesosphere. The discreteness of the representation, and the lack of ray tracing to follow the path of the gravity wave may well exaggerate the shear drag variability.

The convectively generated waves affect the tropical mesosphere. The properties of these waves such as their dominant wavelength, phase velocity and amplitude

are not well known. As parameterized here they have momentum fluxes similar to shear waves, and thus generally break at high levels. The large phase velocities associated with penetrating convection do appear to be necessary to decelerate the easterlies at levels near and above the stratopause; smaller-phase velocity waves are trapped by critical levels below. This problem could be circumvented in the real atmosphere if waves generated at other latitudes refract to the equatorial region. However, the expected refraction distances based on our preliminary ray-tracing experiments are only several thousand kilometers (several model grid boxes); Schoeberl (1985b) noted that long refraction distances are unlikely, due to the intense damping that would occur in the process. As discussed in the Introduction, high phase velocity waves are continually seen in the mesosphere, and the values assigned here are definitely within range of observations. It does appear as if the parameterized convective waves may be exaggerating the equatorial oscillations that appear in the model; they do not cause these oscillations, which were apparent in the model 1 version, and appear to represent inertial instability phenomena.

b. Effect of the model top

As indicated in Fig. 14, the model top definitely plays a role in influencing model results at the highest levels. The boundary condition of zero vertical velocity exaggerates the eddy vertical heat transport divergence, and cools the atmosphere. To alleviate this problem we have allowed all the parameterized gravity-wave momentum flux which reaches the top level to be deposited in that level, which increases the kinetic energy dissipation and provides additional heating of about 30%. This procedure still does not allow the model to produce warm enough temperatures, and the effect worsened in the sensitivity experiments when different momentum sources were removed. When the top was moved to other altitudes, the eddy sensible heat divergence increased in the other top layers. There are at least three ways to alleviate this problem. The most obvious is to move the top to even higher levels; the problem may remain, but it will be out of the mesosphere. In regions above 90 km, tides, ionic phenomena, atmospheric inhomogeneities and nonlocal thermodynamic equilibria may become more prevalent, which will complicate modeling efforts. The dissipation at upper levels could also be increased; this will eliminate the eddies responsible for the heat flux divergence, an effect which does work in the model. However, the added dissipation also reduces the mean zonal winds at upper levels, which may already be slightly too weak (Fig. 3). It would be useful to know what the actual eddy energy is near the mesopause, to test the model dissipation in the mesosphere. It is also possible that increasing the number of vertical layers at the top might diminish the problem; however, Miyahara et al. (1986),

using the GFDL model with 40 layers in the vertical, still found it necessary to incorporate a Rayleigh friction to damp waves at the model top.

c. Effect of increased resolution

The GCMAM results shown here were obtained with a relatively coarse resolution ($8^\circ \times 10^\circ$). It might be expected that several of the model deficiencies could be alleviated with a higher resolution version. In particular, the long-wave energy in the troposphere and stratosphere might increase, as indicated in Table 3. However, the changes in long-wave energy between the nine-layer fine-grid and medium-grid models is not dramatic. It is our experience that the primary impact of higher resolution is to improve the slope of the energy spectrum by diminishing the intermediate wave energy. In the GISS models, the $4^\circ \times 5^\circ$ resolution version has less eddy energy overall, although its eddy transports are as good or better than the coarser model, and some features such as the polar lows and subtropical highs are better resolved (Hansen et al., 1983). Modeling groups have often found that the major characteristic of high-resolution models, run sufficiently long to establish their climatology, is an increase in the zonal wind speed. High-resolution models are not cure-alls for problems of long-wave generation.

If the equatorial oscillations are inertial in nature, then the instability sets in when $(f - \delta \bar{U}/\delta y)$ is less than zero in the Northern Hemisphere. With smaller values of δy available in finer resolution models, smaller values of δU would set off the instability, so increased resolution might result in a smoother equatorial wind field. Additional questions concerning the influence of model resolution are more subtle: although the model generates what appear to be reasonable dynamic events, the cascade of energy or potential enstrophy to the highest wavenumbers has to be different in a coarse-grid model than in the real world. It is unclear what effect this difference would have on stratospheric processes, although it should at least affect the appearance of the "tongues" of high potential vorticity (and tracers) advected out of the polar vortex (McIntyre and Palmer, 1984).

What about the question of vertical resolution? The tropical tropopause in the model is not quite cold enough possibly because the layering does not coincide with the location of the coldest observed temperatures. We noted earlier that the GCMAM was run with a specified water vapor mixing ratio of 3×10^{-6} above 100 mb. However, we did keep track of the actual water vapor in the model, which was initiated at this value throughout the stratosphere and mesosphere. By the end of the five-year run the water vapor values above 100 mb had approximately doubled. It is conceivable that this effect would have been minimized were higher vertical resolution to be used, but several experiments

tried with increased vertical resolution had little obvious effect on the overall simulation. Subtle effects such as wave growth and phase variation with altitude may prove responsive to increased resolution, although the layering used in this model is smaller than a scale height. Increasing the layering near the model top might help minimize the problem of the cold upper layer by limiting the magnitude of the divergence, but the overall problem will still exist. As discussed in the Introduction, to generate gravity waves directly and properly will require very fine vertical as well as horizontal resolution, an accurate numerical scheme, and, ultimately, direct generation of convective events.

6. Conclusions

We have attempted to show in this paper that a coarse-grid model with a gravity wave parameterization based on linear theory and sources controlled by model-produced variables could generate a realistic troposphere-stratosphere-mesosphere model for use in climate/middle atmosphere studies. There exist other gravity wave schemes involving nonlinear parameterizations which include a turbulent nonlinear damping increment related to the wave amplitude (Weinstock, 1982); nevertheless, the model as constituted produces reasonable simulations of the mean wind and temperature fields, and eddy energy, as well as realistic variability of these parameters. In this regard it is important to note that the dissipation induced by the parameterized waves appears appropriate both from the energy budget perspective and in comparison with that employed in other models. The vertical diffusion induced by the breaking waves also compares well with expectations. As better definition of gravity-wave properties becomes available, the parameterizations can be made more realistic.

The chief model deficiencies are 1) temperatures too cold near the top of the model and too warm in the Southern Hemisphere winter polar lower stratosphere, 2) long-wave amplitudes about 30% too small in the lower stratosphere, 3) and inertial-type oscillations in the tropical wind field near the stratopause which may or may not be realistic. The long-wave characteristics and inertial oscillation magnitude may be altered with finer resolution, while raising the model top may be the necessary long-term solution for any middle-atmosphere model.

With $8^\circ \times 10^\circ$ resolution and 23 layers, the GCMAM runs faster than the nine-level model with $4^\circ \times 5^\circ$ resolution. It is thus feasible to use it for long-term integrations, which are necessary to obtain estimates of climate change impacts on the stratosphere and stratospheric feedbacks to climate change. As will be shown in Part II, the model also produces a realistic degree of variability that is especially important in this regard; it also implies that the model displays the proper

consistency of the parameterized gravity-wave drag. Additional improvements, such as the use of higher resolution, should be tested to identify which processes will improve. Ultimately, all experiments must be done on as high a resolution as practical; parameterized gravity-wave drag, like parameterized convection, must be viewed as an expedient until greater computer power and better knowledge of the relevant physical and numerical processes are available.

Acknowledgments. We thank J. Hansen for generously supplying the needed facilities and computer time, and P. Stone, M. Prather, R. Lindzen, W. Robinson and K. Takano for useful discussions during the course of this work. V. Oinas provided thermal radiation line-by-line calculations for comparison with the model radiation scheme. M. Hitchman and N. McFarlane gave helpful recommendations in review. Funding was provided by the NASA Upper Atmospheric Research Program managed by D. Butler, and the ERBS/SAGE II Science Program through NASA Langley Research Center.

REFERENCES

- Allen, M., Y. Yung and J. Waters, 1981: Vertical transport and photochemistry in the terrestrial mesosphere and lower thermosphere (50–120 km). *J. Geophys. Res.*, **86**, 3617–3627.
- Andrews, D. G., and M. E. McIntyre, 1978: Generalized Eliassen-Palm and Charney-Drazin theorems for waves on axisymmetric mean flows in compressible atmosphere. *J. Atmos. Sci.*, **35**, 175–185.
- Arakawa, A., 1972: Design of the UCLA general circulation model. Tech. Rep. No. 7, Dept. of Meteorology, University of California, Los Angeles, 116 pp.
- , and V. R. Lamb, 1977: Computational design of the basic dynamical processes of the UCLA general circulation model. *Methods in Computational Physics*, Vol. 17, Academic Press, 337 pp.
- Balachandran, N. K., 1980: Gravity waves from thunderstorms. *Mon. Wea. Rev.*, **108**, 804–816.
- , and W. L. Donn, 1964: Short and long-period gravity waves over the northeast United States. *Mon. Wea. Rev.*, **92**, 423–426.
- Balsley, B. B., W. L. Ecklund and D. C. Fritts, 1983: VHF echoes from the high-latitude mesosphere and lower thermosphere: observations and interpretations. *J. Atmos. Sci.*, **40**, 2451–2466.
- Barnett, J. J., and M. Corney, 1985a: Middle atmosphere reference model derived from satellite data. *MAP*, **16**, 47–85. [Available from SCOSTEP Secretariat, University of Illinois, 1406 W. Green Street, Urbana, Illinois 61801.]
- , and —, 1985b: Planetary waves, climatological distribution. *MAP*, **16**, 86–137. [Available from SCOSTEP Secretariat, University of Illinois, 1406 W. Green Street, Urbana, Illinois 61801.]
- Bedard, A. J. Jr., F. Canavero and F. Einaudi, 1986: Atmospheric gravity waves and aircraft turbulence encounters. *J. Atmos. Sci.*, **43**, 2838–2844.
- Blumen, W., 1972: Geostrophic adjustment. *Rev. Geophys. Space Phys.*, **10**, 485–528.
- Boer, G. J., N. A. McFarlane, R. Laprise, J. D. Henderson and J.-P. Blanchet, 1984: The Canadian Climate Centre spectral atmospheric general circulation model. *Atmos.-Ocean*, **22**, 397–429.
- Bosart, L., and J. Cussen, 1973: Gravity mean phenomena accompanying east coast cyclogenesis. *Mon. Wea. Rev.*, **101**, 446–454.
- Boville, B. A., 1985: The influence of damping on the winter lower stratosphere. *J. Atmos. Sci.*, **42**, 904–916.

- , and W. J. Randel, 1986: Observations and simulations of the variability of the stratosphere and troposphere in January. *J. Atmos. Sci.*, **43**, 3015–3034.
- Chao, W. C., and M. R. Schoeberl, 1984: On the linear approximation of gravity wave saturation in the mesosphere. *J. Atmos. Sci.*, **41**, 1893–1898.
- Crane, A., J. Haigh, J. Pyle and C. Rogers, 1980: Mean meridional circulation of the stratosphere and mesosphere. *Pure Appl. Geophys.*, **118**, 307–328.
- Defant, F., A. Osthaus and P. Speth, 1979: The global energy budget of the atmosphere. Part II: The ten-year mean structure of the stationary large-scale wave disturbances of temperature and geopotential height for January and July (Northern Hemisphere). *Contrib. Atmos. Phys.*, **52**, 229–246.
- Dell'osso, L., 1984: High-resolution experiments with the ECMWF Model: A case study. *Mon. Wea. Rev.*, **112**, 1853–1883.
- Dickinson, R. E., E. C. Ridley and R. G. Roble, 1984: Thermospheric general circulation with coupled dynamics and composition. *J. Atmos. Sci.*, **41**, 205–219.
- Dopplnick, T., 1971: The energetics of the lower stratosphere including radiative effects. *Quart. J. Roy. Meteor. Soc.*, **97**, 209–237.
- Dunkerton, T., 1978: On the mean meridional mass motions of the stratosphere and mesosphere. *J. Atmos. Sci.*, **35**, 2325–2333.
- , 1981: On the inertial stability of the equatorial middle atmosphere. *J. Atmos. Sci.*, **38**, 2354–2364.
- Dutsch, H. U., 1971: Photochemistry of atmospheric ozone. *Advances in Geophysics*, Vol. 15, Academic Press, 219–315.
- , 1974: The ozone distribution in the atmosphere. *Can. J. Chem.*, **52**, 1491–1504.
- Ebel, A., 1984: Contributions of gravity waves to the momentum, heat and turbulent energy budget of the upper mesosphere and lower thermosphere. *J. Atmos. Terr. Phys.*, **46**, 727–737.
- Fels, S. B., 1982: A parameterization of scale-dependent radiative damping rates in the middle atmosphere. *J. Atmos. Sci.*, **39**, 1141–1152.
- Frank, W. M., 1983: The cumulus parameterization problem. *Mon. Wea. Rev.*, **111**, 1859–1871.
- Fritts, D. C., 1984: Gravity wave saturation in the middle atmosphere: a review of theory and observations. *Rev. Geophys. Space Phys.*, **22**, 275–308.
- , B. B. Balsey and W. L. Ecklund, 1984: VHF echoes from the arctic mesosphere and lower thermosphere. Part II: Interpretations. *Dynamics of the Middle Atmosphere*, J. R. Holton and T. Matsuno, Eds., Terra, 97–116.
- Garcia, R. R., and J. E. Geisler, 1974: Vertical structure of stationary planetary waves in the presence of altitude-dependent zonal winds and dissipation. *J. Geophys. Res.*, **79**, 5613–5623.
- Gartner, V., and M. Memmesheimer, 1984: Computation of the zonally-averaged circulation driven by heating due to radiation and turbulence. *J. Atmos. Terr. Phys.*, **46**, 755–765.
- Gates, W. L., and A. B. Nelson, 1974: A new (revised) tabulation of Scripps topography on a 1° global grid. Part I: Terrain heights. Rep R-1276-1-ARPA, Rand Corporation, Santa Monica, CA., 132 pp.
- Geller, M., M.-F. Wu and M. Gelman, 1983: Troposphere-stratosphere (Surface–55 km) monthly winter general circulation statistics for the Northern Hemisphere—four-year averages. *J. Atmos. Sci.*, **40**, 1334–1352.
- , —, 1984: Troposphere-stratosphere (surface–55 km) monthly winter general circulation statistics for the Northern Hemisphere—interannual variations. *J. Atmos. Sci.*, **41**, 1726–1744.
- Ghazi, A., 1976: Ozone and stratospheric temperatures. *J. Geophys. Res.*, **81**, 5365–5373.
- Gille, J. C., and L. V. Lyjak, 1986: Radiative heating and cooling rates in the middle troposphere. *J. Atmos. Sci.*, **43**, 2215–2229.
- Gregory, J., C. Meek and A. Manson, 1981: Mean zonal and meridional wind profiles for the mesosphere and lower thermosphere at 52°N, $L = 4.4$, during solar maximum. *Atmos.-Ocean*, **19**, 24–34.
- Groves, G., 1971: Atmospheric structure and its variations in the region from 25 to 120 km. AFCRL-71-0410, Env. Res. Pap. No. 368. Hanscom AFB, Bedford, MA. [Available from NTIS N772-24459.]
- Hansen, J., G. Russell, D. Rind, P. Stone, A. Lacis, S. Lebedeff, R. Ruedy and L. Travis, 1983: Efficient three-dimensional global models for climate studies: models I and II. *Mon. Wea. Rev.*, **111**, 609–662.
- Hartmann, D., 1977: Dynamic studies of the Southern Hemisphere stratosphere. *COSPAR Space Research*, **XVII**, 167–174.
- , C. R. Mechoso and K. Yamazaki, 1984: Observations of wave-mean flow interactions in the Southern Hemisphere. *J. Atmos. Sci.*, **41**, 351–362.
- Hayashi, Y., and D. G. Golder, 1985: Nonlinear energy transfer between stationary and transient waves simulated by a GFDL spectral general circulation model. *J. Atmos. Sci.*, **42**, 1340–1350.
- Hines, C. O., 1960: Internal gravity waves at ionospheric heights. *Can. J. Phys.*, **38**, 1441–1481.
- Hirota, I., 1976: Waves in the stratosphere. *Quart. J. Roy. Meteor. Soc.*, **102**, 757–770.
- , 1980: Observational evidence of the semiannual oscillation in the tropical middle atmosphere—a review. *Pure Appl. Geophys.*, **118**, 217–238.
- , 1984: Climatology of gravity waves in the middle atmosphere. *Dynamics of the Middle Atmosphere*, J. R. Holton and T. Matsuno, Eds., Terra, 767–773.
- Holton, J. R., 1975: *The Dynamic Meteorology of the Stratosphere and Mesosphere*. Meteor. Monogr., **15**, Amer. Meteor. Soc., 216 pp.
- , 1982: The role of gravity wave-induced drag and diffusion in the momentum budget of the mesosphere. *J. Atmos. Sci.*, **39**, 791–799.
- , 1983: The influence of gravity wave breaking on the general circulation of the middle atmosphere. *J. Atmos. Sci.*, **40**, 2497–2507.
- Hopkins, R., 1975: Evidence of polar-tropical coupling in upper-stratospheric zonal wind anomalies. *J. Atmos. Sci.*, **32**, 712–719.
- Hunt, B., 1981: The maintenance of the zonal mean state of the upper atmosphere as represented in a three-dimensional general circulation model extending to 100 km. *J. Atmos. Sci.*, **38**, 2172–2186.
- Istok, M. J., and L. V. Doviak, 1986: Analysis of the relation between Doppler spectral width and thunderstorm turbulence. *J. Atmos. Sci.*, **43**, 2199–2214.
- Itoh, H., 1985: The role of transient motions in the formation of quasi-stationary planetary waves. *J. Atmos. Sci.*, **42**, 917–932.
- Johnson, F. S., and E. M. Wilkins, 1965: Correction to “thermal limit on eddy diffusion in the mesosphere and upper thermosphere.” *J. Geophys. Res.*, **70**, 4063.
- Kasahara, A., and T. Sasamori, 1974: Simulation experiments with a 12-layer stratospheric global circulation model. II. Momentum balance and energetics in the stratosphere. *J. Atmos. Sci.*, **31**, 408–421.
- Keliher, T. E., 1975: The occurrence of microbarograph-detected gravity waves compared with the existence of dynamically unstable wind shear layers. *J. Geophys. Res.*, **80**, 2967–2976.
- Kida, H., 1984: A numerical experiment on the general circulation of the middle atmosphere with a three-dimensional model explicitly representing internal gravity waves and their breaking. *Pure Appl. Geophys.*, **122**, 731–746.
- Klemp, J. B., and D. K. Lilly, 1978: Numerical simulation of hydrostatic mountain waves. *J. Atmos. Sci.*, **35**, 78–107.
- Koshelkov, Y., 1977: Monthly mean temperatures, pressures and densities in the stratosphere of the Southern Hemisphere, 25–50 km. *COSPAR Space Research*, **XVII**, 123–130.
- Labitzke, K., 1974: The temperature in the upper stratosphere: difference between hemispheres. *J. Geophys. Res.*, **79**, 2171–2175.
- , 1980: Climatology of the stratosphere and mesosphere. *Phil. Trans. Roy. Soc. London*, **A296**, 7–18.

- , 1981: Stratospheric-mesospheric midwinter disturbances: a summary of observed characteristics. *J. Geophys. Res.*, **86**, 9679–9687.
- , and J. Barnett, 1973: Global time and space changes of satellite radiances received from the stratosphere and lower mesosphere. *J. Geophys. Res.*, **78**, 483–496.
- , and B. Goretzki, 1982: A catalogue of dynamic parameters describing the variability of the middle stratosphere during the northern winters. *MAP*, **5**, C. Sechrist, Jr., Ed., 188 pp. [Available from the SCOSTEP Secretariat, University of Illinois, 1406 W. Green Street, Urbana, Illinois 61801.]
- Lacis, A., and J. E. Hansen, 1974: A parameterization for the absorption of solar radiation in the Earth's atmosphere. *J. Atmos. Sci.*, **31**, 118–133.
- , P. Lee, T. Mitchell and S. Lebedeff, 1981: Greenhouse effect of trace gases, 1970–1980. *Geophys. Res. Lett.*, **8**, 1035–1038.
- Larsen, M. F., W. E. Swartz and R. F. Woodman, 1982: Gravity-wave generation by thunderstorms observed with a vertically pointing 430 MHz radar. *Geophys. Res. Lett.*, **9**, 571–574.
- Lilly, D. K., and P. J. Kennedy, 1973: Observations of a stationary mountain wave pattern and its associated momentum flux and energy dissipation. *J. Atmos. Sci.*, **30**, 1135–1152.
- , and P. F. Lester, 1974: Waves and turbulence in the stratosphere. *J. Atmos. Sci.*, **31**, 800–812.
- Lindzen, R. S., 1981: Turbulence and stress due to gravity wave and tidal breakdown. *J. Geophys. Res.*, **86**, 9707–9714.
- , 1984: Gravity waves in the middle atmosphere. *Dynamics of the Middle Atmosphere*, J. R. Holton and T. Matsuno, Eds., Terra, 3–18.
- , 1985: Multiple gravity-wave breaking levels. *J. Atmos. Sci.*, **42**, 301–305.
- Lipps, F. B., and R. S. Hemler, 1986: Numerical simulation of deep tropical convection associated with large-scale convergence. *J. Atmos. Sci.*, **43**, 1796–1816.
- London, J., 1980: Radiative energy sources and sinks in the stratosphere and mesosphere. *Proc. of the NATO Advanced Study Institute on Atmospheric Ozone*, A. C. Aiken, Ed., Rep. No. FAA-EE-80-20, U.S. Dept. of Transportation, 703–721.
- , R. D. Bojkov, S. Oltmans, and J. I. Kelley, 1976: *Atlas of the Global Distribution of Total Ozone July 1957–June 1967*. NCAR Tech. Note 113 + Str, 276 pp.
- London, J., J. Frederick and G. Anderson, 1977: Satellite observations of the global distribution of stratospheric ozone. *J. Geophys. Res.*, **82**, 2543–2556.
- Mahlman, J. D., and L. J. Umscheid, 1984: Dynamics of the middle atmosphere: Successes and problems of the GFDL “SKYHI” general circulation model. *Dynamics of the Middle Atmosphere*, J. R. Holton and T. Matsuno, Eds., Terra, 501–526.
- Manabe, S., D. G. Hahn and J. L. Holloway, Jr., 1979: Climate simulations with GFDL spectral models of the atmosphere: effect of spectral truncation. *Report of the JOC study conference on climate models: performance, intercomparison and sensitivity studies. Vol. 1*. W. L. Gates, Ed. GARP Publ. Ser. 22 41–94.
- Matsuno, T., 1982: A quasi one-dimensional model of the middle atmosphere circulation interacting with internal gravity waves. *J. Meteor. Soc. Japan*, **60**, 215–226.
- McCormick, M. P., H. M. Steele, P. Hamill, W. P. Chu and T. J. Swisler, 1982: Polar stratospheric cloud sightings by SAM II. *J. Atmos. Sci.*, **39**, 1387–1397.
- McGregor, J., and W. Chapman, 1979: Stratospheric temperatures and geostrophic winds during 1973–1974. *Quart. J. Roy. Meteor. Soc.*, **105**, 241–261.
- McIntyre, M. E., and T. N. Palmer, 1984: The “surf zone” in the stratosphere. *J. Atmos. Terr. Phys.*, **46**, 825–849.
- Mechoso, C. R., K. Yamazaki, A. Kitoh and A. Arakawa, 1985: Numerical forecasts of stratospheric warming events during the winter of 1979. *Mon. Wea. Rev.*, **113**, 1015–1029.
- Meek, C. E., I. M. Reid and A. H. Manson, 1985: Observations of mesospheric wind velocities. I: Gravity wave horizontal scales and phase velocities determined from spaced wind observations. *Radio Science*, **20**, 1363–1382.
- Mesinger, F., 1982: On the convergence and error problems of the calculation of the pressure gradient force in sigma coordinate models. *Geophys. Astrophys. Fluid Dyn.*, **19**, 105–117.
- Miyahara, S., Y. Hayashi and J. D. Mahlman, 1986: Interactions between gravity waves and planetary-scale flow simulated by the GFDL “SKYHI” general circulation model. *J. Atmos. Sci.*, **43**, 1844–1861.
- Miyakoda, K., G. D. Hembree, R. F. Strickler and I. Shulman, 1972: Cumulative results of extended forecast experiments 1. Model performance for winter cases. *Mon. Wea. Rev.*, **100**, 836–855.
- Naujokat, B., 1981: Long-term variations in the stratosphere of the Northern Hemisphere during the last two sunspot cycles. *J. Geophys. Res.*, **86**, 9811–9816.
- Newell, R., 1968: The general circulation of the atmosphere above 60 km. *Meteor. Monogr.*, No. **31**, Amer. Meteor. Soc., 98–113.
- Oort, A., 1964: On the energetics of the mean and eddy circulations in the lower stratosphere. *Tellus*, **16**, 309–327.
- , and J. P. Peixoto, 1983a: Global angular momentum and energy balance requirements from observations. *Advances in Geophysics*, Vol. 25, Academic Press, 355–490.
- , and J. P. Peixoto, 1983b: *Global Atmospheric Circulation Statistics*. NOAA Prof. Paper 14, U.S. Dept. of Commerce, Washington, D.C., 180 pp.
- Palmer, T. N., G. J. Shutts and R. Swinbank, 1986: Alleviation of a systematic westerly bias in general circulation and numerical weather prediction models through an orographic gravity wave drag parameterization. *Quart. J. Roy. Meteor. Soc.*, **112**, 1001–1040.
- Peltier, W. R., and T. L. Clark, 1979: The evolution and stability of finite-amplitude mountain waves. *J. Atmos. Sci.*, **36**, 1498–1529.
- Pierce, A. D., and S. C. Coroniti, 1966: A mechanism for the generation of acoustic-gravity waves during thunderstorm formation. *Nature*, **210**, 1209–1210.
- Pierrehumbert, R. T., and B. Wyman, 1985: Upstream effects of mesoscale mountains. *J. Atmos. Sci.*, **42**, 977–1003.
- Ramanathan, V., H. B. Singh, R. J. Cicerone and J. T. Kiehl, 1985: Trace gas trends and their potential role in climatic change. *J. Geophys. Res.*, **90**, 5547–5566.
- Rind, D., 1986: The dynamics of warm and cold climates. *J. Atmos. Sci.*, **43**, 3–24.
- , R. Suozzo, A. Lacis, G. Russell and J. E. Hansen, 1984: Twenty-one layer troposphere-stratosphere climate model. NASA Tech Memo 86183, 75 pp.
- , and N. K. Balachandran, 1988: The GISS Global Climate/Middle Atmosphere Model. Part II: Model variability due to interactions between planetary waves, the mean circulation, and gravity waves drag. *J. Atmos. Sci.*, **45**, 371–386.
- Robinson, W. A., 1986: The application of the quasi-geostrophic Eliassen-Palm flux to the analysis of stratospheric data. *J. Atmos. Sci.*, **43**, 1017–1023.
- Russell, G., and J. Lerner, 1981: A new finite-differencing scheme for the tracer transport equation. *J. Appl. Meteor.*, **20**, 1483–1498.
- Sadourny, R., 1975: The dynamics of finite-difference models of the shallow-water equations. *J. Atmos. Sci.*, **32**, 680–689.
- Schlesinger, M. E., and J. F. B. Mitchell, 1985: Model projections of the equilibrium climatic response to increased carbon dioxide. *The Potential Climatic Effects of Increasing Carbon Dioxide*, 81–147, U.S. DOE/ER-0237.
- Schoeberl, M. R., 1985a: The penetration of mountain waves into the middle atmosphere. *J. Atmos. Sci.*, **42**, 2856–2864.
- , 1985b: A ray-tracing model of gravity wave propagation and breakdown in the middle atmosphere. *J. Geophys. Res.*, **90**, 13067–13072.
- Slingo, A., and D. W. Pearson, 1986: A comparison of the impact of an envelope orography and of a parameterization of oro-

- graphic gravity-wave drag on model simulations. British Meteor. Office Dyn. Clim. Tech. Note No. 43, 30 pp.
- Smith, A. K., 1983: Stationary waves in the winter stratosphere: seasonal and interannual variability. *J. Atmos. Sci.*, **40**, 245–261.
- Tenenbaum, J., 1982: Integrated and spectral energetics studies of the GLAS general circulation model. *Mon. Wea. Rev.*, **110**, 962–980.
- van Loon, H., and R. L. Jenne, 1972: The zonal harmonic standing waves in the Southern Hemisphere. *J. Geophys. Res.*, **77**, 992–1003.
- , —, and K. Labitzke, 1973: Zonal harmonic standing waves. *J. Geophys. Res.*, **78**, 4463–4471.
- Vincent, R. A., 1984: Gravity wave motions in the mesosphere. *J. Atmos. Terr. Phys.*, **46**, 119–131.
- , and I. M. Reid, 1983: HF Doppler measurements of mesospheric gravity wave momentum fluxes. *J. Atmos. Sci.*, **40**, 1321–1333.
- Wallace, J. M., and V. E. Kousky, 1968: Observational evidence of Kelvin waves in the tropical stratosphere. *J. Atmos. Sci.*, **25**, 900–907.
- , and J. K. Woessner, 1982: An analysis of forecast error in the NMC hemispheric primitive equation model. *Mon. Wea. Rev.*, **109**, 2444–2449.
- Weinstock, J., 1982: Nonlinear theory of gravity waves: momentum deposition, generalized Rayleigh friction, and diffusion. *J. Atmos. Sci.*, **39**, 1698–1710.
- Wu, M.-F., M. A. Geller, J. G. Olson and M. E. Gelman, 1985: Troposphere–stratosphere (surface–55 km) monthly general circulation statistics for northern hemisphere—four year averages. NASA Tech. Rep. TM 86182, 95 pp.
- Yamamoto, M., T. Tsuda and S. Kato, 1986: Gravity waves observed by the Kyoto meteor radar in 1983–1985. *J. Atmos. Terr. Phys.*, **48**, 597–603.
- Zimmerman, S. P., 1974: The effective vertical turbulent viscosity as measured from radio meteor trails. *J. Geophys. Res.*, **79**, 1095–1098.